An Integrative Model of the Cardiac Ventricular Myocyte Incorporating Local Control of Ca^{2+} Release

Joseph L. Greenstein and Raimond L. Winslow
Department of Biomedical Engineering and The Whitaker Biomedical Engineering Institute, Center for Computational Medicine and Biology, The Johns Hopkins University School of Medicine and Whiting School of Engineering, Baltimore, Maryland 21205 USA

ABSTRACT The local control theory of excitation-contraction (EC) coupling in cardiac muscle asserts that L-type Ca^{2+} current tightly controls Ca^{2+} release from the sarcoplasmic reticulum (SR) via local interaction of closely apposed L-type Ca^{2+} channels (LCCs) and ryanodine receptors (RyRs). These local interactions give rise to smoothly graded Ca^{2+}-induced Ca^{2+} release (CICR), which exhibits high gain. In this study we present a biophysically detailed model of the normal canine ventricular myocyte that conforms to local control theory. The model formulation incorporates details of microscopic EC coupling properties in the form of Ca^{2+} release units (CaRUs) in which individual sarcolemmal LCCs interact in a stochastic manner with nearby RyRs in localized regions where junctional SR membrane and transverse-tubular membrane are in close proximity. The CaRUs are embedded within and interact with the global systems of the myocyte describing ionic and membrane pump/exchanger currents, SR Ca^{2+} uptake, and time-varying cytosolic ion concentrations to form a model of the cardiac action potential (AP). The model can reproduce both the detailed properties of EC coupling, such as variable gain and graded SR Ca^{2+} release, and whole-cell phenomena, such as modulation of AP duration by SR Ca^{2+} release. Simulations indicate that the local control paradigm predicts stable APs when the L-type Ca^{2+} current is adjusted in accord with the balance between voltage- and Ca^{2+}-dependent inactivation processes as measured experimentally, a scenario where common pool models become unstable. The local control myocyte model provides a means for studying the interrelationship between microscopic and macroscopic behaviors in a manner that would not be possible in experiments.

INTRODUCTION

Understanding of the mechanisms by which Ca^{2+} influx via voltage-gated L-type Ca^{2+} channels (LCCs) triggers Ca^{2+} release from the junctional sarcoplasmic reticulum (SR) has advanced tremendously with the development of experimental techniques for simultaneous measurement of LCC currents and Ca^{2+} transients (Wier et al., 1994; Cannell et al., 1987; Nabauer et al., 1989), and detection of local Ca^{2+} transients (Cannell et al., 1984; Lopez-Lopez et al., 1994, 1995; Cheng et al., 1995). This has given rise to the local control theory of excitation-contraction (EC) coupling (Stern, 1992; Bers, 1993; Wier et al., 1994; Sham, 1997), which asserts that opening of an individual LCC located in the transverse (T) tubular membrane triggers Ca^{2+} release from a small cluster of SR Ca^{2+} release channels known as ryanodine receptors (RyRs) located in the closely apposed junctional SR membrane (Fabiato, 1985; Cheng et al., 1993; Cannell et al., 1995; Santana et al., 1996, Sham et al., 1995; Collier et al., 1999; Wang et al., 2001). Tight regulation of this Ca^{2+}-induced Ca^{2+} release (CICR) is made possible by the fact that LCCs and RyRs are sensitive to local rather than global Ca^{2+} levels. The local control theory also asserts that graded control of SR Ca^{2+} release, in which Ca^{2+} release from junctional SR is a smooth, increasing function of Ca^{2+} influx, is achieved by statistical recruitment of elementary SR Ca^{2+} release events by trigger Ca^{2+} entering via single LCCs (Stern, 1992; Beuckelmann and Wier, 1988; Wier and Balke, 1999). In addition to triggering SR Ca^{2+} release, increases of local Ca^{2+} promote Ca^{2+}-dependent inactivation of LCCs (Peterson et al., 1999; Bers and Perez-Reyes, 1999). Because L-type Ca^{2+} current (I_{CaL}) plays a primary role in determining action potential (AP) shape and duration, local control theory therefore implies that the microscopic properties of Ca^{2+} release are likely to contribute to macroscopic electrophysiological responses of the cardiac myocyte.

Several computational models have been developed to investigate properties of local Ca^{2+} release at the level of the cardiac dyad (Rice et al., 1999; Stern et al., 1999; Langer and Peskoff, 1996; Cannell and Soeller, 1997; Soeller and Cannell, 1997). Each of these model formulations incorporates 1) one or a few LCCs; 2) a cluster of RyRs; 3) the dyadic volume in which the events of CICR occur; and 4) anionic binding sites, which buffer Ca^{2+}. In some of these models, detailed descriptions of diffusion and Ca^{2+} binding in the dyadic cleft are used to demonstrate the effects of geometry, LCC, and RyR properties and organization, and surface charge on the spatiotemporal profile of Ca^{2+} within the dyad, and hence on the efficiency of CICR (Langer and Peskoff, 1996; Cannell and Soeller, 1997; Soeller and Cannell, 1997). Stern et al. (1999) have simulated CICR stochastically using numerous RyR schemes to demonstrate conditions necessary for stability of EC coupling, and have suggested a possible role for allosteric interactions between RyRs. The functional release unit model of Rice et al. (1999) has demonstrated that local

Submitted December 14, 2001, and accepted for publication July 26, 2002.
Address reprint requests to Raimond L. Winslow, Clark Hall, Room 201B, 3400 N. Charles St., Baltimore, MD 21218. Tel.: 410-516-5417; Fax: 410-516-5294; E-mail: rwinslow@bme.jhu.edu.

0006-3495/02/12/2918/28 $2.00

control of CICR (i.e., graded SR release and high EC coupling gain) can be obtained without including computationally intensive descriptions of Ca^{2+} gradients within the dyadic space. Isolated EC coupling models such as these, however, cannot elucidate the nature of the interaction between local events of CICR and integrative cellular behavior.

Existing models of the cardiac ventricular myocyte do not incorporate mechanisms of local control of SR Ca^{2+} release (Winslow et al., 1999; Jafri et al., 1998; Luo and Rudy, 1994; Priebe and Beuckelmann, 1998; Pandit et al., 2001; Noble et al., 1998; Fox et al., 2002). Rather, in these models all Ca^{2+} influx through sarcolemmal LCCs and Ca^{2+} release flux through RyRs is directed into a common Ca^{2+} compartment. As defined by Stern (1992), a "common pool" model is one in which trigger Ca^{2+} reaches the SR via the same cytosolic Ca^{2+} pool into which SR Ca^{2+} is released, where activation of the SR release mechanism is controlled by Ca^{2+} concentration in this cytosolic pool. The result of this physical arrangement is that once RyR Ca^{2+} release is initiated, the resulting increase of Ca^{2+} concentration in the common pool stimulates regenerative, all-or-none rather than graded Ca^{2+} release (Stern, 1992). This "latch up" of Ca^{2+} release can be avoided, and graded SR release can be achieved in a model of EC coupling by formulating Ca^{2+} release flux as an explicit function of sarcolemmal Ca^{2+} influx (Priebe and Beuckelmann, 1998; Luo and Rudy, 1994; Faber and Rudy, 2000; Fox et al., 2002). Models of this type are not common pool models based on the definition given by Stern (1992), and do not suffer an inability to stably exhibit both high gain and graded SR Ca^{2+} release. These phenomenological formulations, however, lack mechanistic descriptions of the processes that are the underlying basis of CICR. Both common pool models and models with phenomenological Ca^{2+} release mechanisms are therefore inadequate for the study of how detailed microscopic features of EC coupling have an impact on macroscopic electrophysiological properties of the myocyte, such as the whole-cell Ca^{2+} transient and AP morphology.

In this study, we develop a comprehensive model of the ventricular myocyte based on the theory of local control of SR Ca^{2+} release. This is accomplished by updating and extending the canine ventricular myocyte model of Winslow et al. (1999) to include a population of dyadic Ca^{2+} release units. Local interactions of individual sarcolemmal LCCs with nearby RyRs in the JSR membrane are simulated stochastically, with these local simulations embedded within the numerical integration of the differential equations describing ionic and membrane pump/exchanger currents, SR Ca^{2+} cycling, and time-varying cytosolic ion concentrations. We demonstrate that this model faithfully reproduces experimentally observed features of LCC voltage- and Ca^{2+}-dependent gating (Linz and Meyer, 1998; Sipido et al., 1995; Hobai and O'Rourke, 2001; Sham et al., 1995; Sham, 1997; Rose et al., 1992; Herzig et al., 1993), microscopic EC coupling (Wier et al., 1994; Sham et al., 1998; Song et al., 2001), and macroscopic whole-cell AP and Ca^{2+} cycling properties (O'Rourke et al., 1999). Simulations demonstrate that local control is an essential property for stability of APs when the LCC inactivation process depends more strongly on local Ca^{2+} than on membrane potential, a scenario that is supported by experiments (Linz and Meyer, 1998; Peterson et al., 1999, 2000), but which cannot be implemented successfully using a common pool model where the inherent positive feedback of rising Ca^{2+} levels on RyR activation is intact. Modeling supports the hypothesis that the robust bidirectional interaction between Ca^{2+} dynamics and membrane potential in the local control environment plays a central role in establishing the integrative electrophysiological properties of the cardiac myocyte. Preliminary results from this study were presented previously in abstract form (Greenstein and Winslow, 2001a, 2001b).

METHODS

The Ca^{2+} release unit model

We seek to define a model of local control of SR Ca^{2+} release that captures fundamental properties such as graded release, while at the same time is computationally tractable such that it may be incorporated into an integrative model of the ventricular myocyte. Models describing diffusion of Ca^{2+} within the dyadic space, detailed dyad geometry, and surface charge effects (Cannell and Soeller, 1997; Soeller and Cannell, 1997; Langer and Peskoff, 1996) are too computationally demanding for this application. As a compromise between structural and biophysical detail versus tractability, a "minimal model" of local control of Ca^{2+} release, referred to as the Ca^{2+} release unit (CaRU) model, is implemented. A full mathematical description of the stochastic state models, dynamical equations, parameters, and initial conditions defining the myocyte model are given in Appendix I.

Fig. 1 *A* shows a schematic of the CaRU model based in part on the previous model of Rice et al. (1999). The CaRU model is intended to mimic the properties of Ca^{2+} sparks in the T-tubule/SR (T-SR) junction. Ca^{2+} sparks are elementary SR Ca^{2+} release events arising from a cluster of RyRs (Cheng et al., 1993). Fig. 1 *B* shows a cross-section of the model T-SR cleft, which is divided into four individual dyadic subspace compartments arranged on a 2×2 grid. Each subspace (SS) compartment contains a single LCC and 5 RyRs in its JSR and sarcolemmal membranes, respectively. All 20 RyRs in the CaRU (5 RyRs/SS $\times$ 4 SSs/CaRU $=$ 20 RyRs/CaRU) communicate with a single local JSR volume. The 5:1 RyR/LCC stoichiometry is chosen to be consistent with recent estimates indicating that a single LCC typically triggers the opening of four to six RyRs (Wang et al., 2001). Each subspace is treated as a single compartment in which Ca^{2+} concentration is uniform; however, Ca^{2+} may diffuse passively to neighboring subspaces within the same CaRU. The rate of Ca^{2+} transfer between two adjacent subspace compartments is assumed to be 10-fold slower than that from subspace to cytosol. This yields an inter-subspace transfer rate (r_{iss}) of 20 ms^{-1}, which corresponds to a diffusion coefficient of $\sim 3.3 \times 10^{-6}$ cm^2 s^{-1} when the assumed height of the model subspace is 12 nm. This value is similar to estimates for Ca^{2+} diffusion in the presence of RyR "feet" structures in the restrictive dyadic subspace volume (Soeller and Cannell, 1997). The division of the CaRU into four subunits allows for the possibility that an LCC may trigger Ca^{2+} release in adjacent subspaces (i.e., RyR recruitment) under conditions where unitary LCC currents are large. The existence of communication

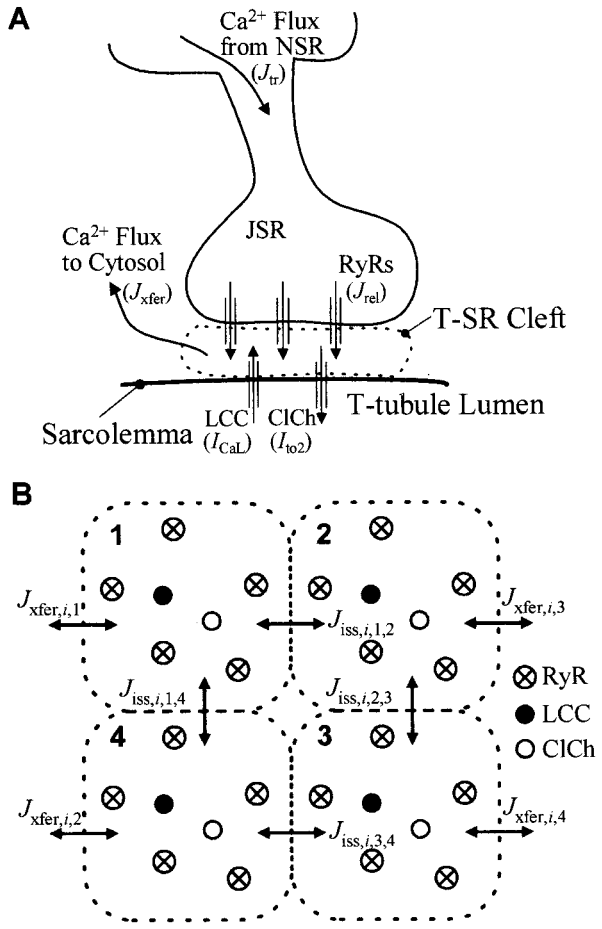

FIGURE 1 Schematic representation of the Ca^{2+} release unit model (CaRU). (*A*) Trigger Ca^{2+} influx through the LCCs enters into the T-SR cleft (dyadic space). The rise in local Ca^{2+} level promotes the opening of RyRs and ClChs. The excess local Ca^{2+} passively diffuses out of the cleft into the cytosol, and JSR Ca^{2+} is refilled via passive diffusion from the NSR. (*B*) The T-SR cleft (shown in cross-section) is composed of four dyadic subspace volumes, arranged on a 2 × 2 grid, each containing 1 LCC, 1 ClCh, and 5 RyRs. Ca^{2+} in any subspace may diffuse to a neighboring subspace (J_{iss}) or to the cytosol (J_{xfer}). $J_{iss,i,j,l}$ represents Ca^{2+} flux from the *j*th subspace to the *l*th subspace within the *i*th CaRU. Similarly, $J_{xfer,i,j}$ represents Ca^{2+} flux from the *j*th subspace to the cytosol from the *i*th CaRU (see Appendix I).

among adjacent subspace volumes is supported by the findings that Ca^{2+} release sites can be coherent over distances larger than that occupied by a single release site (Parker et al., 1996), and that the mean amplitude of Ca^{2+} spikes, local SR Ca^{2+} release events that consist of one or a few Ca^{2+} sparks (Song et al., 1998), exhibits a bell-shaped voltage dependence, indicating synchronization of multiple Ca^{2+} release events within a T-SR junction (Song et al., 2001). The choice of four subunits allows for semi-quantitative description of dyadic Ca^{2+} diffusion while retaining minimal model complexity.

One of the bases for local control of SR Ca^{2+} release is the structural separation of T-SR clefts at the ends of sarcomeres (i.e., RyR clusters are physically separated) (Franzini-Armstrong et al., 1999). Each CaRU is therefore simulated independently in accord with this observation. Upon activation of RyRs, subspace Ca^{2+} concentration will become elevated. This Ca^{2+} will freely diffuse to either adjacent subspace compartments (J_{iss}) or into the cytosol (J_{xfer}) along its concentration gradient. The local JSR compartment is refilled via passive diffusion of Ca^{2+} from the network SR (NSR) compartment (J_{tr}).

The model for the L-type Ca^{2+} channel is identical in structure to the mode-switching model developed previously by Jafri et al. (1998). The following modifications have been made to model parameters: 1) voltage-dependence of forward and reverse activation transition rates (α and β, respectively) have been adjusted based on recent measurements of I_{CaL} obtained in canine midmyocardial cells (Hobai and O'Rourke, 2001); 2) voltage-independent transition rates into open states f and f' have been adjusted to yield peak open probability in the range of 5–15% in response to a maximally activating voltage clamp stimulus (Rose et al., 1992; Herzig et al., 1993; Handrock et al., 1998); 3) transition rates between the normal gating mode (Mode Normal) and the Ca^{2+}-inactivation mode (Mode Ca) γ and ω are adjusted to enhance Ca^{2+}-dependent inactivation, while the voltage-dependent steady-state inactivation function (y_∞) is modified to have an asymptotic value of 0.6 for large positive membrane potentials. The latter is based on the observation that there is a small sustained component of Ca^{2+} current in response to voltage clamp stimuli in canine ventricular cells (Kääb et al., 1996; Tseng et al., 1987), and that Ca^{2+}-dependent inactivation dominates the I_{CaL} inactivation process while voltage-dependent inactivation is relatively weak and incomplete (Linz and Meyer, 1998; Hadley and Hume, 1987; Peterson et al., 1999, 2000); 4) permeation through the LCC is described by the Goldman-Hodgkin-Katz current equation as originally presented by Luo and Rudy (Luo and Rudy, 1994) where Ca^{2+} concentration at the inner mouth of the channel is assumed to be equivalent to Ca^{2+} concentration of the adjacent subspace, rather than assuming it is constant (Jafri et al., 1998; Rice et al., 1999); 5) LCC permeability (P_{CaL}) is adjusted to a value of 9.13×10^{-13} cm^3 s^{-1}, which yields a single channel slope conductance of 8.2 pS and a unitary current of ~−0.12 pA at 0 mV (see Fig. 2 *G*) (Rose et al., 1992; Yue and Marban, 1990).

Whole-cell Ca^{2+} current can be described as a function of the total number of channels (N_{LCC}), the single channel current magnitude (i), the open probability (p_o), and the fraction of channels that are available for activation (f_{active}, i.e., in a phosphorylated mode), where $I_{CaL} = N_{LCC} \times i \times p_o \times f_{active}$ (Handrock et al., 1998). Under conditions where f_{active} remains constant, $I_{CaL} = N_{active} \times i \times p_o$, where $N_{active} = N_{LCC} \times f_{active}$ is constant. As described above, single channel parameters are based on experimentally obtained constraints on both i and p_o. N_{active} is therefore chosen such that the amplitude of the ensemble current summed over all LCCs corresponds to whole-cell measurements in canine myocytes (Hobai and O'Rourke, 2001). This approach yields a value of 50,000 for N_{active}, which agrees with experimental estimates of LCC density (Rose et al., 1992; McDonald et al., 1986), and which corresponds to 12,500 CaRUs (N_{CaRU}). The process of slow cycling between active and inactive states is not included in this model; rather only active LCCs are simulated.

Each RyR channel is represented by the model developed by Keizer and Smith (1998) and later modified by Rice et al. (1999). This model was originally designed to describe the property of RyR adaptation, a slow spontaneous decrease in open probability that has been observed to occur after activation by a step increase in Ca^{2+} when measured in single channels reconstituted in lipid bilayers (Gyorke and Fill, 1993). A channel in the adapted state can be reactivated by an additional increase in Ca^{2+}. In contrast, the findings of Sham et al. (1998) suggest that RyR inactivation into an absolute refractory state occurs in vivo during EC coupling. It is difficult to incorporate single channel RyR data obtained in vitro into models of EC coupling due to the lack of quantitative information regarding in vivo regulation by accessory proteins and other ligands. Therefore, our approach has been to constrain RyR model parameters based on experimentally obtained properties of EC coupling (Song et al., 2001; Wier et al., 1994), without an explicit attempt to retain the property of adaptation. The Ca^{2+} dependence of the RyR model state transition rates have been adjusted based on the assumption that four Ca^{2+} ions must bind to the channel before it can enter the open state (Zahradnikova et al., 1999).

Ca^{2+} buffering in each CaRU is implemented as described previously (Rice et al., 1999) using the rapid buffer approximation (Wagner and

Keizer, 1994). It is assumed that Ca^{2+} is buffered in the subspace by the phospholipid anion groups on both the SR and sarcolemmal membranes, and that these buffers are immobile (Smith et al., 1998). Buffering parameters for JSR Ca^{2+} are based on measures of Ca^{2+}-calsequestrin binding (Shannon et al., 2000).

The Ca^{2+}-dependent transient outward chloride (Cl^-) current (I_{to2}) is included as part of the CaRU. Experimental evidence indicates that the Ca^{2+} binding affinity of this Cl^- channel (ClCh) is low ($K_{d,ClCh} \sim 150$ μM) relative to normal cytosolic Ca^{2+} concentrations (Collier et al., 1996), and that I_{to2} is abolished in the presence of caffeine and exhibits rate-dependent properties that correlate with those of SR Ca^{2+} load (Zygmunt, 1994), suggesting that ClChs are activated by subspace Ca^{2+}. Estimates of ClCh density are in the range of 3–4 μm^{-2} (Collier et al., 1996), a value similar to the density of active LCCs (2–5 μm^{-2}) (Rose et al., 1992; McDonald et al., 1986). Each CaRU therefore includes an equal number of ClChs as LCCs, i.e., one Cl^- channel per subspace (Fig. 1 *B*). I_{to2} is modeled as a voltage- and time-independent ligand-gated channel, using a simple two-state, closed-open model (see Fig. 12 *C*), based on the gating and permeation properties of the unitary current as measured by Collier et al. (1996). For simplicity, intracellular Cl^- concentration is assumed to be constant.

Whole myocyte model

Definitions for global state variables (e.g., K^+ currents, cytosolic Ca^{2+} concentration) of the local control myocyte model are based on those of the Winslow et al. (1999) canine ventricular cell model with the following modifications: 1) the voltage-dependent Ca^{2+}-independent transient outward potassium (K^+) current (I_{to1}) is modeled as described by Greenstein et al. (2000); 2) the rapid delayed rectifier K^+ current (I_{Kr}) is modeled as described by Mazhari et al. (2001); 3) the SR Ca^{2+} ATPase (SERCA2a pump) has been updated based on the model and parameter set of Shannon et al. (2000), which accounts for both a forward and a backward Ca^{2+} pump flux; and 4) some membrane currents and ionic fluxes are scaled to preserve cytosolic ionic concentrations and AP shape (see Appendix I).

A detailed description of the local control simulation algorithm is given in Appendix II. Within the whole-cell simulation, the time progression of states within each CaRU is calculated individually. The simulation of each CaRU requires both numerical integration of local (subspace and JSR) Ca^{2+} balance equations and Monte Carlo simulation of channel gating (LCC, RyR, and ClCh). The state of each channel is described by a set of discrete valued random variables that evolve in time as described by Markov processes. Time steps for CaRU simulations are adaptive and are chosen to be sufficiently small based on channel transition rates. The CaRU simulations occur within the (larger) time step used for the numerical integration of global state variables (e.g., V_m). The majority of computational time is spent in stochastic simulation of the large number of independent CaRUs. This simulation is therefore highly parallelizable, and is implemented on an SGI Power Challenge symmetric multiprocessing computer configured with 12 R10,000 processors and 1 Gbyte memory.

As a result of the embedded Monte Carlo simulation, all state variables (e.g., V_m) and ionic currents/fluxes (e.g., I_{CaL}) will contain a component of stochastic noise (e.g., Fig. 3 *A*). These fluctuations introduce a degree of variability to simulation output. Therefore, where appropriate, simulation data are presented as mean ± SE, where the specified value for *n* refers to the number of simulation runs.

RESULTS

L-type Ca^{2+} current

Because local control of Ca^{2+} release is the central feature of the myocyte model presented here, it is necessary to verify that the newly parametrized L-type Ca^{2+} channel model behavior is consistent with experimental data for both single LCCs and whole-cell currents. Fig. 2 demonstrates single LCC properties of the model under normal physiological conditions (i.e., with EC coupling intact and 2 mM extracellular Ca^{2+}). Sample LCC unitary currents in response to 200-ms membrane depolarizations to test potentials of −20 mV and 0 mV from a holding potential of −100 mV are shown in Fig. 2, *A* and *B*, respectively. At test pulses ≥0 mV, 200-ms sweeps with no LCC openings seldom occur because 1) no silent mode behavior (Herzig et al., 1993; Handrock et al., 1998) is implemented in this model; 2) voltage-dependent inactivation is relatively slow and incomplete with respect to activation kinetics; and 3) the likelihood that Ca^{2+}-mediated inactivation occurs is very low before the first opening of an LCC. Multiple openings within the same record are common because the steady-state inactivation probability of LCCs at depolarized potentials is substantially less than unity in canine myocytes (i.e., inactivation is incomplete) (Kääb et al., 1996; Tseng et al., 1987; Rose et al., 1992). Fig. 2, *C* and *D* show open time histograms and Fig. 2, *E* and *F* show cumulative first latency distributions, determined at test potentials of −20 mV and 0 mV, respectively, based on a random sampling of 500 LCCs. Open time histograms are well-described by a single exponential (τ_{open} = 0.481 ms and 0.492 ms at −20 mV and 0 mV, respectively), indicating that mean open time does not vary with test potential. Open durations, and first latency distributions are consistent with previous measurements after accounting for differences in experimental conditions (e.g., temperature) (Herzig et al., 1993; Handrock et al., 1998; Schroder et al., 1998; Rose et al., 1992). The fraction of sweeps exhibiting no openings is lower in the model than found in experiments due to the exclusion of LCC silent mode behavior in the model (Handrock et al., 1998). The sharpening of the first latency distribution at depolarized potentials indicates that channel openings become less temporally dispersed with increasing depolarization, in agreement with experimental findings (see Fig. 5 of Rose et al., 1992). Fig. 2 *G* shows unitary currents as a function of membrane potential. Single channel slope conductance, as measured in the range between −80 mV and −20 mV, is 8.2 pS and agrees with measurements made in near physiological solutions (6.9–9.1 pS, see Fig. 3 *B* of Rose et al., 1992, and Fig. 4 *B* of Yue and Marban, 1990).

The summation of all unitary Ca^{2+} currents within the myocyte, such as those shown in Fig. 2, *A* and *B*, yields macroscopic I_{CaL}. Simulated whole-cell currents elicited by a family of depolarizing voltage steps from −30 mV to 40 mV in 10-mV increments are shown in Fig. 3 *A*. Currents activate rapidly (<6 ms) and decay over ~100 ms. In Fig. 3 *B*, peak I_{CaL} amplitude is plotted as function of test potential (where data points represent the mean of five runs at each potential). Maximum inward Ca^{2+} current is produced at a test potential of 10 mV (n = 5). The bell-shaped peak current profile is in close agreement with peak currents

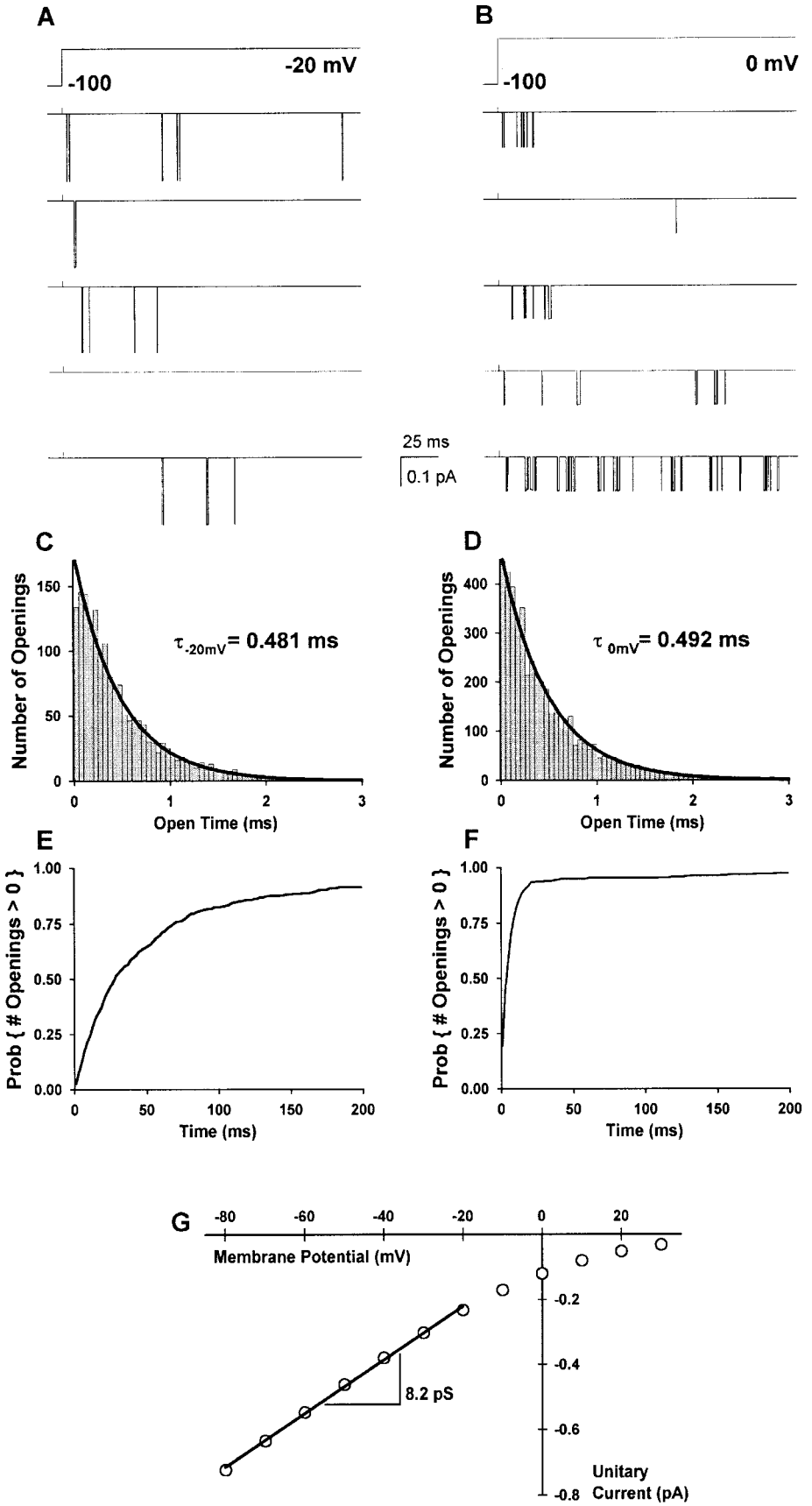

FIGURE 2 Single L-type Ca^{2+} channel model properties. (*A*) and (*B*), sample unitary Ca^{2+} currents in response to a 200-ms test pulse to −20 mV and 0 mV, respectively. The small positive deflection in each current record indicates the time at which voltage is switched to the test potential. (*C*) and (*D*), open duration histograms measured from 500 sweeps at −20 mV and 0 mV, respectively. Exponential fits (*black line*) yield mean open duration of 0.481 ms and 0.492 ms at −20 mV and 0 mV, respectively. (*E*) and (*F*), first latency distribution measured at −20 mV and 0 mV, respectively. (*G*) Single channel current-voltage relation of model LCCs with 2 mM extracellular Ca^{2+}. Unitary conductance is 8.2 pS when measured in the range of −80 mV to −20 mV.

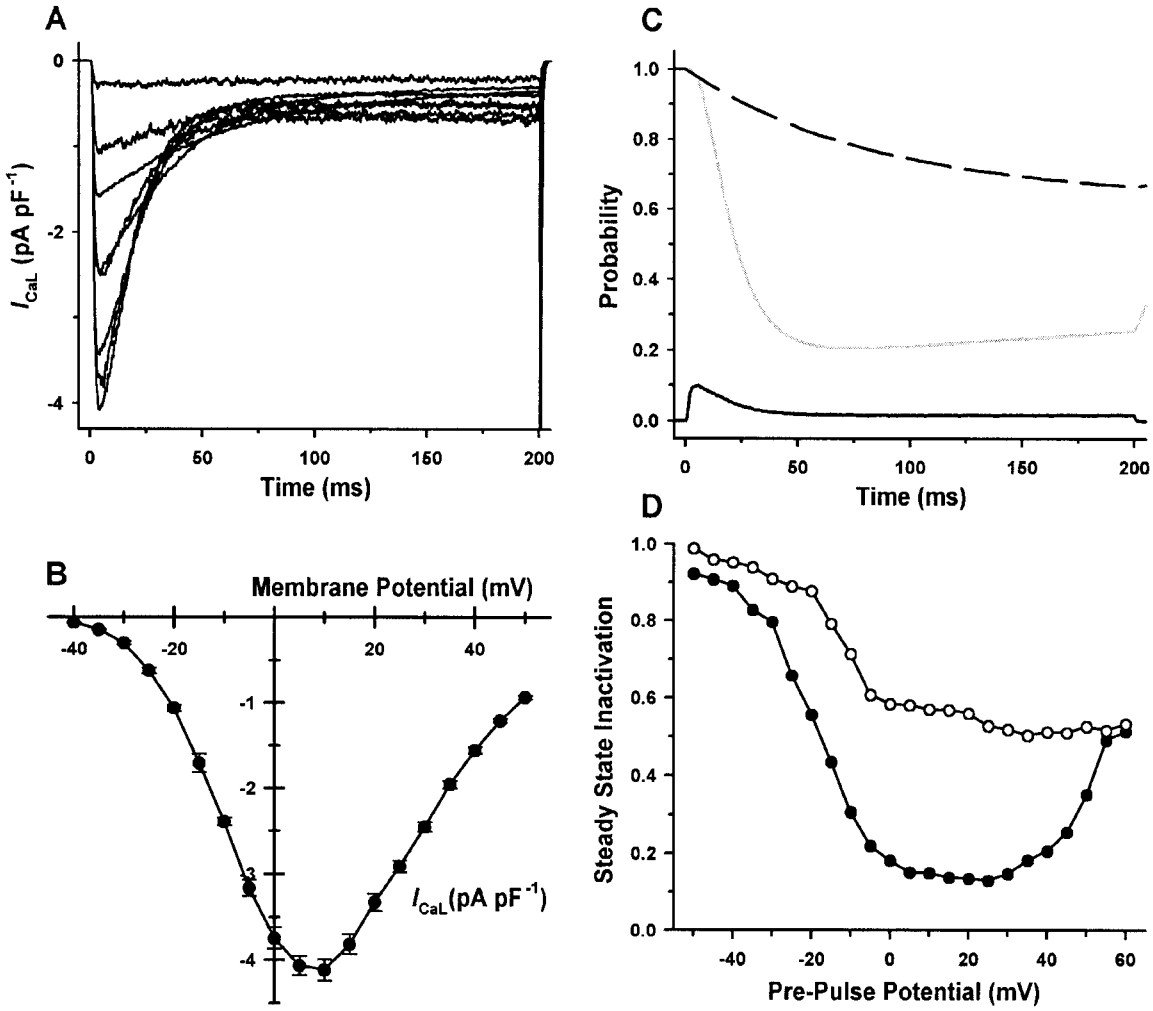

FIGURE 3 Properties of macroscopic I_{CaL}. (*A*) Simulated whole-cell currents as a function of time in response to a family of depolarizing voltage steps from −30 mV to 40 mV in 10 mV increments. (*B*) Mean peak current-voltage relation based on five simulations at each potential (i.e., $n = 5$). (*C*) LCC open probability (*black solid line*), probability of occupancy of Mode Normal (Prob{*Norm*}, *gray solid line*), and probability that voltage-dependent inactivation has not occurred (*y, dashed line*) in response to a voltage clamp to 0 mV. (*D*) Steady-state inactivation curve obtained using a double-pulse protocol (see text) with (*filled circles*) and without (*open circles*) Ca^{2+} as the charge carrier.

measured in canine (compare to Fig. 1 *E* of Hobai and O'Rourke, 2001) (Kääb et al., 1996; O'Rourke et al., 1999), guinea pig (Rose et al., 1992), and human (He et al., 2001) ventricular myocytes. Fig. 3 *C* demonstrates the underlying processes that govern the time course of I_{CaL} during the voltage clamp to 0 mV. The quantities shown are LCC open probability (p_o, *black solid line*), the probability of occupancy of Mode Normal (Prob{*Norm*} = 1 − Prob{Ca^{2+}-mediated inactivation has occurred}, *gray solid line*), and the fraction of channels available for voltage-dependent inactivation (y = 1 − Prob{voltage-dependent inactivation has occurred}, *dashed line*). LCC p_o reaches a peak value of ~0.1, consistent with studies that indicate that peak p_o with Ca^{2+} as the charge carrier (Rose et al., 1992) and time-averaged p_o with Ba^{2+} as the charge carrier (minimizing Ca^{2+}-mediated inactivation) (Herzig et al., 1993; Handrock et al., 1998) is in the range of 0.05–0.15. A comparison of the time progression of Prob{*Norm*} and y clearly demonstrates that at 0 mV, Ca^{2+}-mediated inactivation of I_{CaL} develops more rapidly and progresses more completely than voltage-dependent inactivation, in agreement with recent experiments (Linz and Meyer, 1998; Sipido et al., 1995; Hadley and Hume, 1987; Peterson et al., 1999, 2000). In addition, Ca^{2+}-mediated inactivation is partially relieved in the latter portion of the pulse (Fig. 3 *C*), indicative of decaying local Ca^{2+} levels.

The feedback of local Ca^{2+} signals on LCC gating plays an important role in the determination of properties of both CICR and APs, and is a key feature of the local control myocyte model, which is explored in more detail below. Steady-state inactivation properties of I_{CaL} are measured using a double-pulse protocol where membrane potential is first stepped from

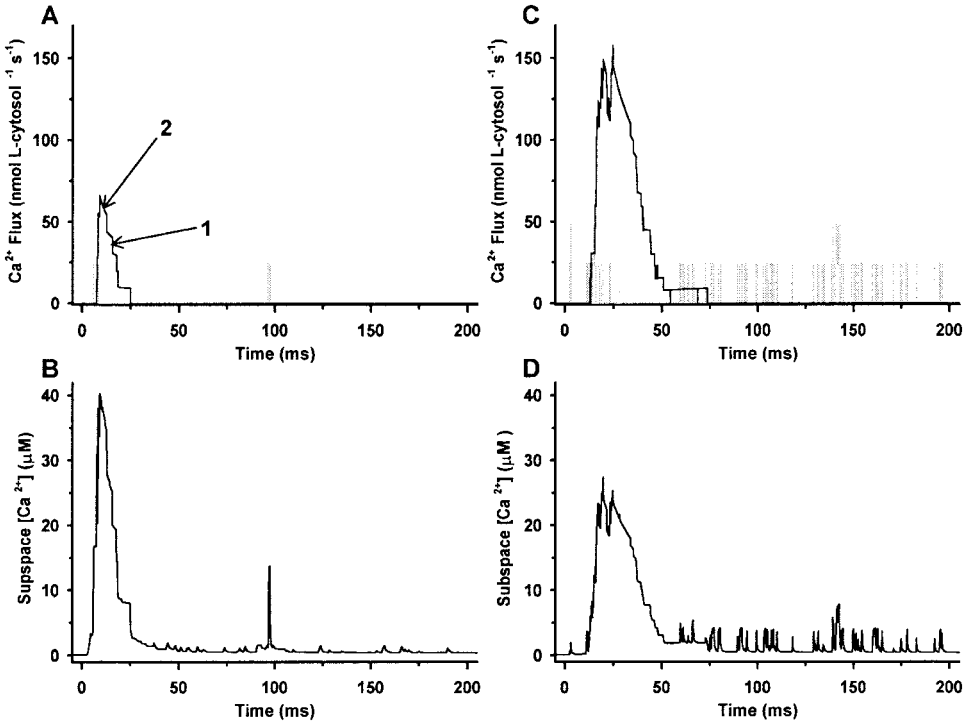

FIGURE 4 Sample results for a single CaRU in response to a 200-ms voltage clamp to 0 mV. (*A*) Ca^{2+} flux through a single LCC (*gray line*) and through the set of five RyRs (*black line*) within a single dyadic subspace compartment. Arrows 1 and 2 highlight changes in SR Ca^{2+} release flux due to changes in the number of open RyRs and due to the changing local Ca^{2+} gradient arising from JSR Ca^{2+} depletion, respectively. (*B*) Subspace Ca^{2+} concentration associated with the events of panel *A*. (*C*) Ca^{2+} flux through the set of four LCCs (*gray line*) and the set of 20 RyRs (*black line*) within a single CaRU. (*D*). Mean subspace Ca^{2+} concentration in the four subspace compartments associated with the events in the CaRU described in panel *C*.

−100 mV to various pre-pulse potentials for 400 ms and then to a 0-mV test potential. Peak currents, normalized by current obtained in the absence of a pre-pulse, are shown as a function of the pre-pulse potential in Fig. 3 *D*. Simulations were performed under normal conditions (*filled circles*) and with subspace Ca^{2+} clamped to diastolic levels to mimic an alternative charge carrier such as Ba^{2+} that would not significantly promote Ca^{2+}-mediated inactivation (*open circles*). Under normal conditions, the I_{CaL} steady-state inactivation curve is U-shaped. Disabling of Ca^{2+}-mediated inactivation yields an inactivation curve that decreases monotonically with depolarization. Inactivation is incomplete, and asymptotically approaches ~50% for highly depolarized pre-pulses. These features agree well with inactivation curves obtained experimentally in native myocytes (compare to Fig. 10 of Hadley and Hume, 1987, Fig. 1 *E* of Linz and Meyer, 1998, and Fig. 7 *B* of Li et al., 1999). Ca^{2+}-mediated inactivation makes a dominant contribution to the total inactivation of I_{CaL} in the range of potentials of −10 mV to +30 mV, consistent with the range of potentials where LCC Ca^{2+} influx is maximal (Fig. 3 *B*). In addition, this is within the range of plateau potentials where inactivation would normally occur during an AP. The U-shape is therefore a consequence of the variation in local Ca^{2+} transients that arise due to the voltage dependence of LCC Ca^{2+} influx, and the subsequent graded CICR.

Excitation-contraction coupling

Fig. 4, *A* and *B*, demonstrate the most elementary model release event, as triggered by a single LCC. A typical response to a 200-ms 0 mV voltage clamp pulse is shown. Ca^{2+} flux through an LCC (*gray line*) and the net SR Ca^{2+} release flux through the five adjacent RyRs (*black line*) are shown in Fig. 4 *A*. At the onset of the voltage pulse, the LCC first opens after ~5 ms, and then exhibits only one additional opening. Local JSR release flux is triggered by the first LCC opening and lasts ~20 ms, far longer than the LCC open duration. The amplitude of the release flux varies with the number of open RyRs and the local Ca^{2+} gradient across the JSR membrane. Individual RyR channel gating events can be discerned as step-like changes in local JSR release flux (Fig. 4 *A, arrow 1*), while changes due to the time varying local Ca^{2+} gradient across the RyRs (i.e., effects of JSR depletion) occur more gradually over time (Fig. 4 *A, arrow 2*). Mean RyR open time varies from ~7 ms, when subspace Ca^{2+} is high early in the voltage clamp pulse to <1 ms after the subspace Ca^{2+} has subsided later in the pulse (data not shown), similar to values reported previously (Rice et al., 1999; Lukyanenko et al., 1996). Fig. 4 *B* shows the corresponding dyadic subspace Ca^{2+} concentration, which reaches a peak value of ~40 μM. The small amplitude deflections in subspace Ca^{2+} level that continue to occur following termination of the transient are the result of inter-subspace Ca^{2+} diffusion (J_{iss}), and are indicative of trigger events (LCC openings) occurring in neighboring subspace compartments within the CaRU.

A local Ca^{2+} spike (a localized Ca^{2+} release event within a single T-SR junction) is modeled by a single CaRU in Fig. 4, *C* and *D*, for the same voltage clamp stimulus. Total Ca^{2+} influx through the set of four LCCs (*gray line*) and the net

SR Ca^{2+} release flux through the set of 20 RyRs (*black line*) are shown in Fig. 4 *C*. LCC Ca^{2+} influx rises to a level consistent with two open channels within a short time following the initiation of the pulse, indicating some degree of temporal synchronization in the onset of trigger Ca^{2+} influx at 0 mV. Net JSR Ca^{2+} release flux follows a similar time course to that observed in an individual subspace. The spatial average of Ca^{2+} concentration in the four subspace compartments of the CaRU is intended to represent a Ca^{2+} spike (Fig. 4 *D*). The peak amplitude of this signal is less than that seen in a single subspace (Fig. 4 *B*) due to temporal dispersion of Ca^{2+} release events. The Ca^{2+} spike duration is ~25 ms (at half-maximal amplitude), similar to that measured in myocytes using confocal imaging techniques (20–50 ms) (Cheng et al., 1993; Song et al., 2001; Sham et al., 1998).

Whole cell Ca^{2+} signals, which can be explained as the spatial and temporal summation of local elementary Ca^{2+} release events, are shown in Fig. 5. Total LCC Ca^{2+} influx (*gray line*) and RyR Ca^{2+} release flux (*black line*) in response to a 0 mV voltage clamp are plotted as a function of time in Fig. 5 *A*. EC coupling gain, measured as the ratio of peak RyR Ca^{2+} flux to peak LCC Ca^{2+} flux, is ~12 at 0 mV. Although peak Ca^{2+} flux through both RyRs and LCCs occurs within a few milliseconds following the onset of the voltage pulse, there is a relatively small sustained component of flux that lasts throughout the duration of the voltage clamp, indicative of a small number of release events associated with LCC reopenings and/or late openings. Fig. 5 *B* demonstrates mean subspace free Ca^{2+} concentration (*solid line*) averaged over all CaRUs, and bulk cytosolic Ca^{2+} concentration (*dashed line*). The peak amplitude of mean subspace Ca^{2+} concentration is ~18 μM, substantially greater than the cytosolic Ca^{2+} level, which peaks at <1 μM. The mean subspace Ca^{2+} concentration is, however, less than that observed for individual simulated Ca^{2+} release events due to temporal dispersion in the occurrence of Ca^{2+} release events, and because Ca^{2+} release fails to occur in some CaRUs. On average, the local Ca^{2+} transient displays fast kinetics. It rises and decays within ~70 ms at 0 mV, while the cytosolic Ca^{2+} transient lasts $\gg$200 ms. The late sustained Ca^{2+} fluxes shown in Fig. 5 *A* give rise to a similar sustained component of the subspace Ca^{2+} signal, which lasts for the duration of the voltage clamp pulse. Fig. 5 *C* shows corresponding free Ca^{2+} levels in the JSR (*solid black line*, average over all JSR volume compartments) and NSR (*solid gray line*), and total SR Ca^{2+} load (*dashed line*), which includes both free and buffer-bound Ca^{2+} in all SR compartments. JSR and NSR Ca^{2+} pools are at similar levels at all times during the pulse, indicative of the fast Ca^{2+} diffusion rate between these compartments (τ_{tr} = 3 ms). Preceding the pulse, SR free Ca^{2+} concentration is ~730 μM, which corresponds to total SR Ca^{2+} content of ~118 μmol L-cytosol^{-1}, in agreement with measurements of SR load in canine myocytes

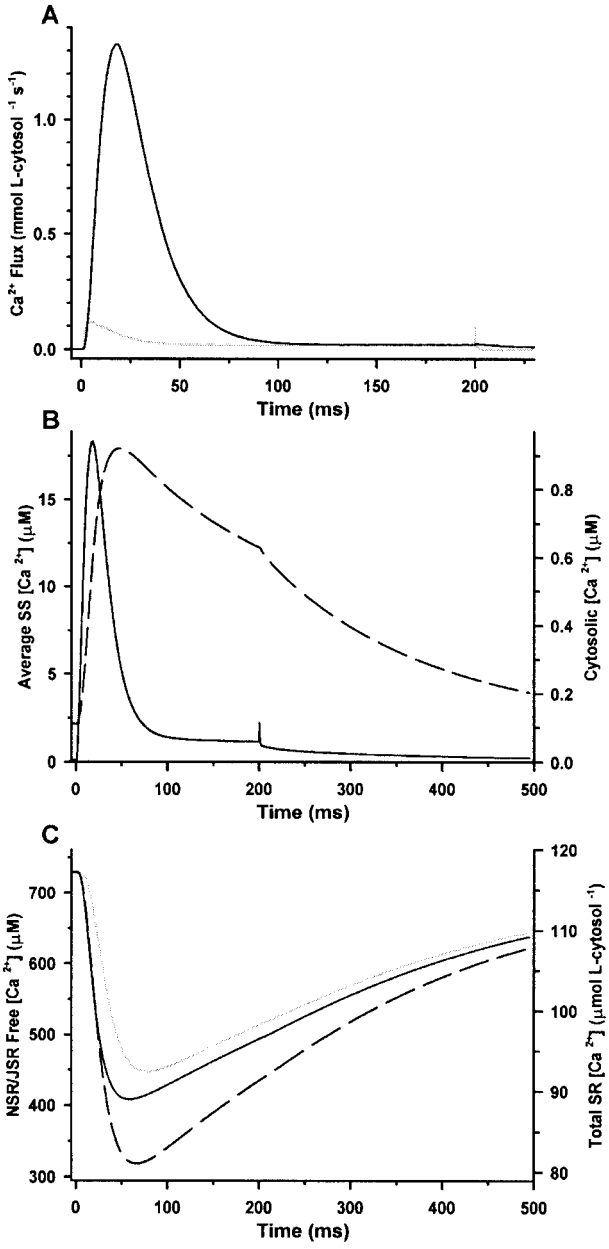

FIGURE 5 Whole-cell Ca^{2+} fluxes and concentrations in response to a 200-ms voltage clamp to 0 mV. (*A*) Ca^{2+} fluxes through the entire population of LCCs (*gray line*) and the entire population of RyRs (*black line*) are shown as a function of time. For consistency, fluxes are reported in units of mmol L-cytosol^{-1} s^{-1} (*B*) Average subspace Ca^{2+} transient (*black line*, left axis) and bulk cytosolic Ca^{2+} transient (*dashed line*, right axis). (*C*) Free Ca^{2+} concentration in the NSR (*gray solid line*, left axis), mean free JSR Ca^{2+} concentration (averaged over all CaRUs, *black solid line*, left axis), and total SR Ca^{2+} concentration (includes both free and bound Ca^{2+} in the NSR and JSR, *dashed line*, right axis).

(Hobai and O'Rourke, 2001). Upon CICR, total SR Ca^{2+} is reduced to ~80 μmol L-cytosol^{-1}, resulting in ~32% decrease in total SR Ca^{2+} content. Similar values of fractional SR Ca^{2+} release have been obtained in experiments (~35%) (Bassani et al., 1995; DelBridge et al., 1996).

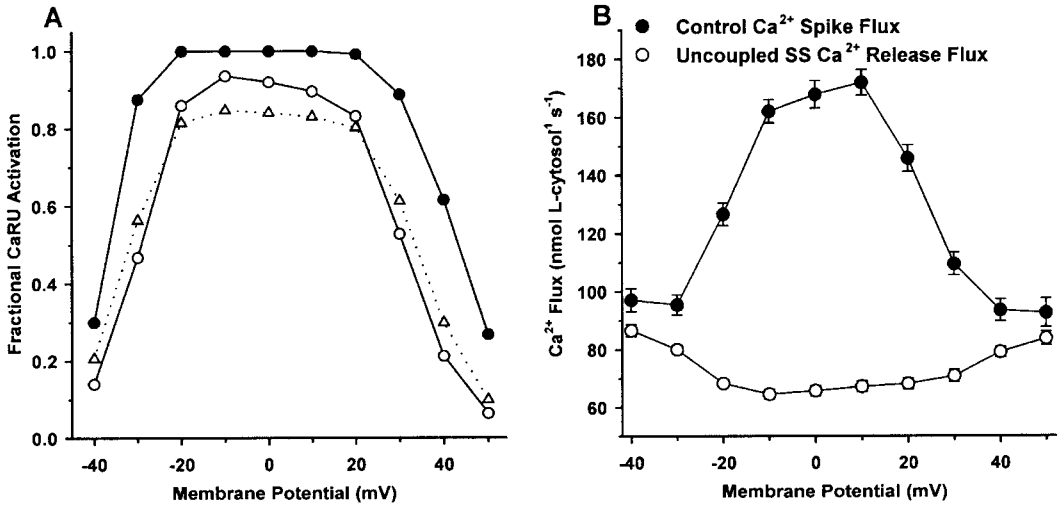

FIGURE 6 Microscopic properties of model Ca^{2+} spikes. (*A*) The fraction of CaRUs that fire a Ca^{2+} spike as a function of voltage under control conditions is shown (*filled circles*). For the modified model lacking intersubspace diffusion, the fraction of subspaces that exhibit a Ca^{2+} release event is shown (*open circles*). The fraction of CaRUs that fire a Ca^{2+} spike in the presence of LCC slow cycling between active and silent modes is estimated (see text, *triangles*), $n \geq 250$ simulations at each potential. (*B*) Ca^{2+} spike amplitude as a function of voltage clamp potential under control conditions (*filled circles*) and for the modified model lacking intersubspace diffusion (*open circles*).

Recently, Song et al. (2001) examined voltage-dependent recruitment and amplitude of Ca^{2+} spikes. Under control conditions, they found a bell-shaped voltage dependence for the likelihood of Ca^{2+} spike occurrence and a shallower bell-shaped dependence for the amplitude of Ca^{2+} spikes. These data demonstrated that the gradation of SR Ca^{2+} release is predominantly attributable to graded recruitment of T-SR junctions, with a smaller contribution due to variations in the amplitude of local Ca^{2+} release flux. Fig. 6 demonstrates the ability of the local control myocyte model to reproduce these findings. Fig. 6 *A* shows the fraction of CaRUs that fire at least one Ca^{2+} spike during a 200-ms depolarizing test pulse as a function of test pulse potential. Ca^{2+} spikes are detected by monitoring the mean subspace Ca^{2+} concentration within each CaRU, and are considered to have occurred if Ca^{2+} concentration rises above a threshold value of 4 μM for a time greater than 5 ms. Values reported in Fig. 6 were determined by analyzing a minimum of 250 CaRUs at each potential ($n \geq 250$). Under control conditions (*filled circles*), the model voltage dependence of the probability of firing a Ca^{2+} spike is bell-shaped and saturates at $\sim$1.0 in the range of -20 mV to $+20$ mV, indicating that it is extremely rare for SR release not to occur in this voltage range. The same simulations were performed using an altered version of the model in which there is a single dyadic subspace per unit (total number of LCCs, RyRs, and subspace compartments per myocyte being conserved) and therefore lacks inter-subspace diffusion (*open circles*). These results represent the probability of elementary release events within the model, and peak at $\sim$0.9 in the range of -10 mV to $+10$ mV. In either case, the bell-shaped voltage dependence indicates that gradation of SR Ca^{2+} release arises, in part, from voltage-dependent recruitment of T-SR junction (i.e., CaRU) activation. If it is assumed that the results for the modified model are similar to the properties of a single subunit within a control CaRU and that CaRU activation (i.e., a Ca^{2+} spike) occurs as long as at least one elementary release event occurs within a CaRU, then the probability of CaRU activation in the presence of LCC silent mode behavior can be estimated. The estimate assumes that only 40% of LCCs are active at any given time ($f_{active} = 0.4$) (Handrock et al., 1998) and produces peak fractional T-SR activation similar to experiments (Song et al., 2001), as shown in Fig. 6 *A* (*triangles*). Fig. 6 *B* shows the model voltage dependence of local Ca^{2+} spike amplitude (as CaRU Ca^{2+} release flux) averaged over all CaRUs for the same two simulations. For the control case (*closed circles*), Ca^{2+} spike amplitude has a shallow bell-shaped voltage dependence and peaks at $\sim$170 nmol L-cytosol^{-1} s^{-1} in the range of -10 mV to $+10$ mV. The rise in mean Ca^{2+} spike amplitude in the central voltage range occurs as a result of enhanced synchronization of RyR release events within CaRUs contributing to gradation of SR Ca^{2+} release, and agrees well with the experiments of Song et al. (2001). In the modified model lacking inter-subspace Ca^{2+} diffusion (*open circles*), subspace Ca^{2+} release flux is smaller at all potentials. This is the case because these signals represent SR Ca^{2+} release flux from a set of five RyRs, whereas the control simulations represent flux from all 20 RyRs in the CaRU. More interesting however, is that the shape of the voltage dependence of the Ca^{2+} transient amplitude in the absence of inter-subspace coupling is inverted compared to the control simulations. In the absence of inter-subspace coupling, synchronization

within a single unit is not possible because only a single Ca^{2+} release event occurs. There is therefore no enhancement of local Ca^{2+} release signals in the central range of potentials. The depressed release at central voltages in the modified model is due to a reduction in the Ca^{2+} gradient across the SR membrane as a result of SR depletion. In the central voltage range, where SR release is maximal (Fig. 6 *A, open circles*), reduction in global SR Ca^{2+} load over the duration of the pulse will lead to a reduction in Ca^{2+} transient amplitude for events that occur late within the pulse (data not shown). In the control case, this effect is masked by the enhancement of Ca^{2+} spike amplitude that occurs within the same range of potentials due to synchronization of release events within CaRUs.

While Fig. 6 shows results regarding voltage-dependent gradation of SR Ca^{2+} release at the level of the CaRU, Fig. 7 demonstrates the macroscopic properties of SR Ca^{2+} release. Previous experimental studies (Wier et al., 1994; Santana et al., 1996; Janczewski et al., 1995; Cannell et al., 1995) and mathematical models (Stern, 1992; Stern et al., 1999) have shown that there can be significant differences between the voltage dependence of LCC Ca^{2+} influx (F_{LCC}) and RyR Ca^{2+} release flux (F_{RyR}) even though SR Ca^{2+} release is controlled by Ca^{2+} entry via I_{CaL}. These differences underlie the phenomenon of "variable" EC coupling gain. We use the definition of gain given by Wier et al. (1994) as the ratio $F_{RyR(max)}/F_{LCC(max)}$. Fig. 7 *A* shows the voltage dependence of $F_{LCC(max)}$ (*filled circles*) and $F_{RyR(max)}$ (*open circles*) obtained using the same voltage protocols as in Fig. 3 *B*. In Fig. 7 *B*, the peak fluxes of Fig. 7 *A* have been normalized based on their respective maxima. Although both $F_{LCC(max)}$ and $F_{RyR(max)}$ are bell-shaped functions of membrane potential, they do not share identical voltage dependence. Maximal LCC Ca^{2+} influx occurs at 10 mV, whereas maximal RyR Ca^{2+} release flux occurs at 0 mV. EC coupling gain as defined above is plotted as a function of voltage in Fig. 7 *C* (*triangles*), and is monotonically decreasing with increasing membrane potential. The similarity in shape of the EC coupling gain curve and the unitary LCC current-voltage relation (*dashed line*, scaled for comparison) suggests that EC coupling gain may be more closely related to unitary LCC current, rather than macroscopic I_{CaL}. The simulated data of Fig. 7 agrees well with experimentally obtained measurements of whole-cell Ca^{2+} fluxes (Wier et al., 1994; Santana et al., 1996; Song et al., 2001; Cannell et al., 1995; Janczewski et al., 1995). The value of r_{iss} (inter-subspace Ca^{2+} transfer rate) was chosen to match the model gain function with experiments and to be consistent with estimates of Ca^{2+} diffusion within the dyad (Soeller and Cannell, 1997). The role of inter-subspace coupling on gain is demonstrated in Fig. 7 *C*, by comparison of control simulations (*triangles*) to those in the absence of inter-subspace coupling (i.e., $r_{iss} = 0$, *squares*). With inter-subspace coupling intact, EC coupling gain is greater at all potentials, but the increase in gain is most dramatic at more negative potentials. In this negative voltage range LCC p_o is submaximal, leading to sparse LCC openings. However,

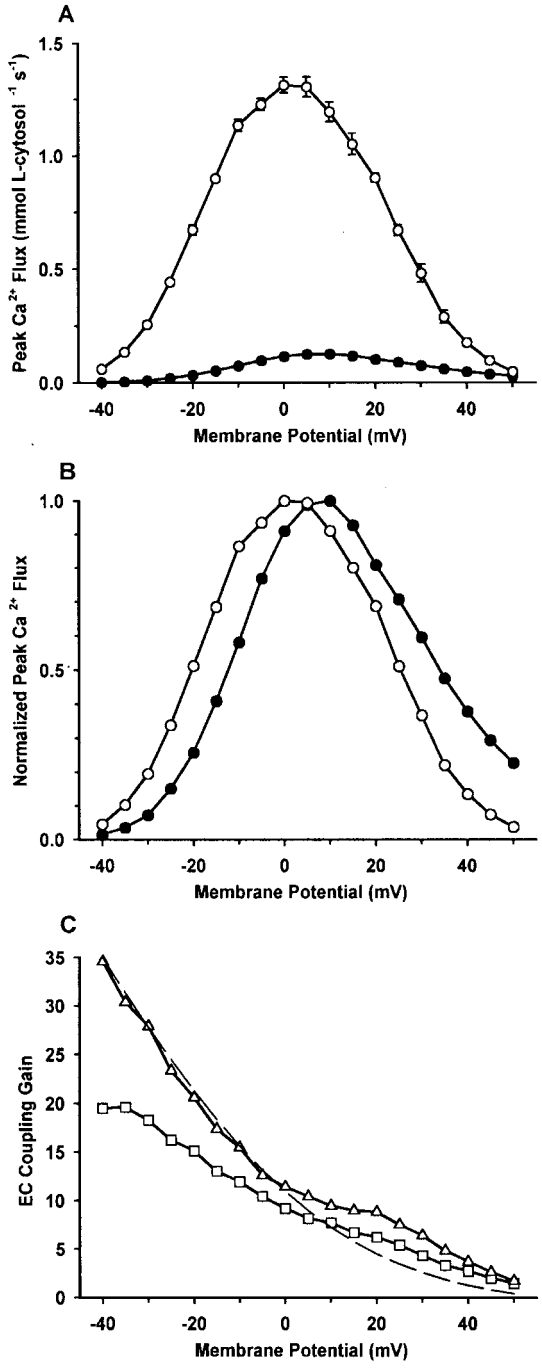

FIGURE 7 Voltage dependence of macroscopic LCC Ca^{2+} influx, SR Ca^{2+} release, and EC coupling gain. (*A*) Mean peak Ca^{2+} flux amplitudes, $F_{LCC(max)}$ (*filled circles*) and $F_{RyR(max)}$ (*open circles*) as a function of membrane voltage, $n = 5$ simulations at each voltage. (*B*) Peak Ca^{2+} fluxes (data of panel *A*) normalized by their respective maxima. (*C*) EC coupling gain as a function of membrane potential defined as $F_{RyR(max)}/F_{LCC(max)}$ under control conditions (*triangles*) and in the absence of inter-subspace coupling within the CaRUs (*squares*), as well as L-type unitary current (*dashed line*, scaled to match the gain function at −40 mV).

unitary current magnitude is relatively high, such that the opening of an LCC efficiently triggers adjacent RyRs. An increased r_{iss} value allows the rise in local Ca^{2+} due to the triggering action a single LCC to recruit and activate RyRs in adjacent subspace compartments within the same T-SR junction (where the LCCs have not opened, as openings are sparse), effectively raising the functional RyR/LCC ratio. The net effect of inter-subspace coupling is to increase the magnitude and slope of the gain function preferentially in the negative voltage range. The local control myocyte model predicts that Ca^{2+} diffusion in the T-SR junction (across the subspace compartments) is an important mechanism underlying the rate at which gain decreases with increasing voltage. Previous models of EC coupling have similarly achieved a steeply decreasing gain function with high amplitude at negative potentials by incorporating details of spatial Ca^{2+} gradients in the dyadic space (Stern et al., 1999).

One defining difference between a macroscopic model and a local control model of EC coupling is that it would be impossible for a macroscopic model to exhibit different values of gain for macroscopic L-type Ca^{2+} currents of the same amplitude (Stern, 1992). Wier et al. (1994) have explicitly demonstrated that Ca^{2+} currents of similar shape and amplitude can evoke very different responses of SR Ca^{2+} release. The local control myocyte model can reproduce the findings of this experiment, as shown in Fig. 8. Fig. 8, *A* and *B* show F_{LCC}, and Fig. 8, *C* and *D* show F_{RyR} in response to 200-ms depolarizing pulses to −20 mV and +50 mV, respectively. Although the amplitude and time course of macroscopic LCC Ca^{2+} influx is similar for the two test pulses, the SR Ca^{2+} release is triggered effectively in response to the −20 mV pulse (where gain is high), but only minimal Ca^{2+} release occurs at +50 mV (where gain is low). In addition, upon repolarization to −100 mV from +50 mV, the brief Ca^{2+} tail current triggers substantial SR Ca^{2+} release (Fig. 8 *D*).

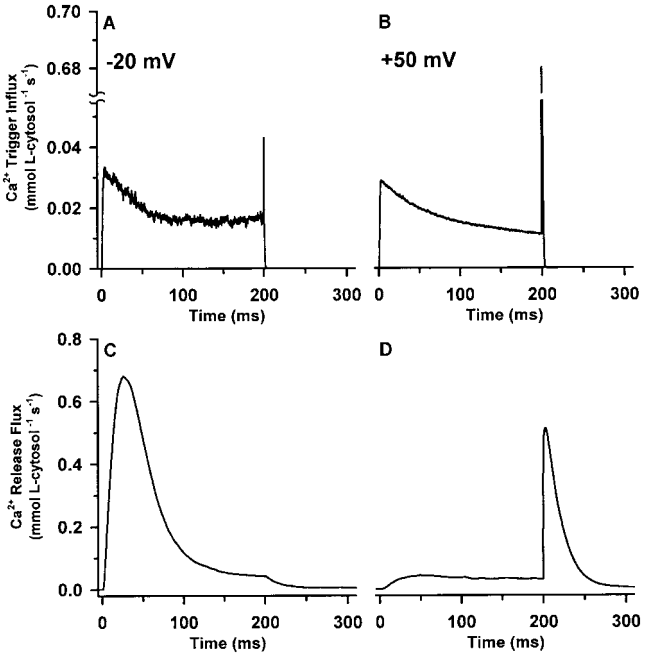

FIGURE 8 Variable EC coupling gain. (*A*) and (*B*), whole-cell LCC Ca^{2+} influx (F_{LCC}) in response to voltage clamp stimuli of −20 mV and +50 mV, respectively. (*C*) and (*D*), whole-cell SR Ca^{2+} release flux (F_{RyR}) in response to voltage clamp stimuli of −20 mV and +50 mV, respectively. Note that while F_{LCC} is similar in response to each of the two voltage clamp stimuli, the magnitude of F_{RyR} is very different, indicating that EC coupling gain is not determined by properties of macroscopic I_{CaL}. In addition, note that the large, but brief, tail of Ca^{2+} influx that occurs following repolarization from +50 mV triggers substantial SR Ca^{2+} release flux.

Action potentials

Fig. 9 demonstrates the ability of the model to reconstruct action potentials and Ca^{2+} transients of normal canine mid-myocardial ventricular myocytes. In Fig. 9 *A*, a normal 1-Hz steady-state AP is shown. AP properties are similar to those measured in experiments (O'Rourke et al., 1999), with action potential duration (APD) of ~300 ms. Fig 9 *B* shows cytosolic (*black line*) and mean subspace (*gray line*) Ca^{2+} transients. While the cytosolic Ca^{2+} transient peaks at ~0.75 μM, and lasts longer than the duration of the AP, Ca^{2+} in the subspace reaches ~11 μM on average, and equilibrates to near-cytosolic levels rapidly, within ~100–150 ms. Fig. 9 *C* demonstrates the two model currents that communicate directly with the local subspaces within the CaRUs, I_{CaL} (*black line*) and I_{to2} (*gray line*). I_{CaL} peaks at ~4.7 pA pF^{-1} and has a sustained component of ~0.7 pA pF^{-1}, which lasts for nearly the entire duration of the AP. I_{to2} peaks at ~0.6 pA pF^{-1} and also displays a minimal sustained current component. The sustained current appears because subspace Ca^{2+} remains moderately elevated on average throughout the AP due to LCC reopenings, and because I_{to2} does not inactivate.

While macroscopic I_{CaL} shown in Fig. 9 *C* has a similar shape as that of the common pool Winslow et al. (1999) canine myocyte model, the underlying LCC inactivation process in the local control model has been altered to depend more strongly on local Ca^{2+} than on membrane potential. This adjustment is based on experimental findings obtained from both isolated myocytes (Linz and Meyer, 1998; Sipido et al., 1995) and recombinant channels expressed in HEK 293 cells (Peterson et al., 1999, 2000), which show that LCC voltage-dependent inactivation is slow and incomplete while Ca^{2+}-mediated inactivation is strong and dominates the inactivation process (see also Fig. 3 *D*). Strong Ca^{2+}-dependent inactivation (in the absence of strong voltage-dependent inactivation) is a key mechanism in determining how graded SR Ca^{2+} release influences AP properties and whole-cell Ca^{2+} dynamics. Fig. 10 demonstrates the differences in I_{CaL} inactivation properties be-

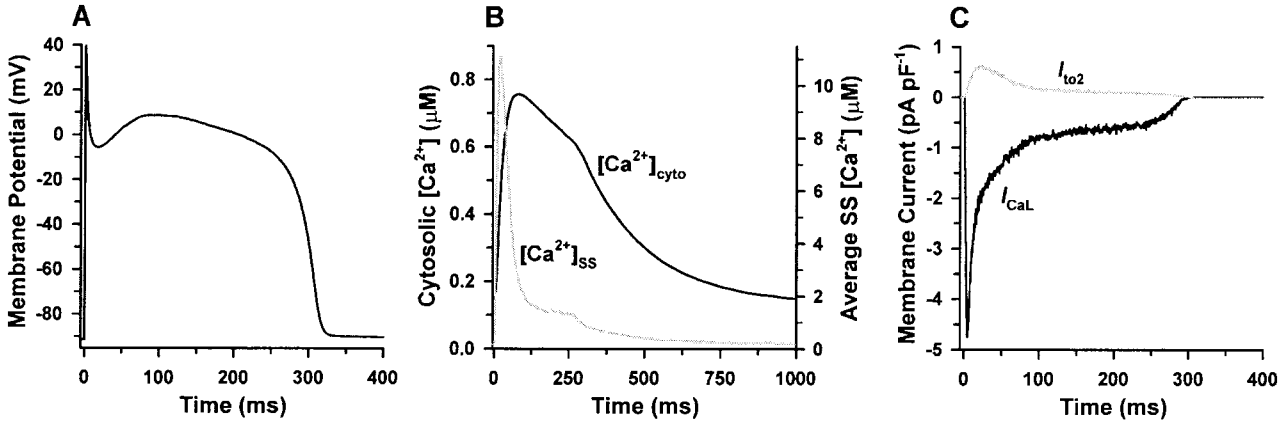

FIGURE 9 The action potential, Ca^{2+} transients, and membrane currents. Signals shown are in response to a 1-Hz pulse train, with responses shown in steady state. (*A*) Membrane potential as a function of time simulated using the local control myocyte model under normal conditions. (*B*) Cytosolic (*black line*, left axis) and mean subspace (*gray line*, right axis) Ca^{2+} concentrations corresponding to the AP simulated in panel *A*. (*C*) L-type Ca^{2+} current (I_{CaL}, *black line*) and the Ca^{2+}-dependent transient outward Cl^- current (I_{to2}, *gray line*) corresponding to the AP simulated in panel *A*.

tween the Winslow et al. (1999) common pool model and the local control myocyte model, and their consequences. Fig. 10, *A* and *B*, show steady-state APs (*solid line*), Prob{*Norm*} (*dashed line*), and *y* (*dotted line*), for the

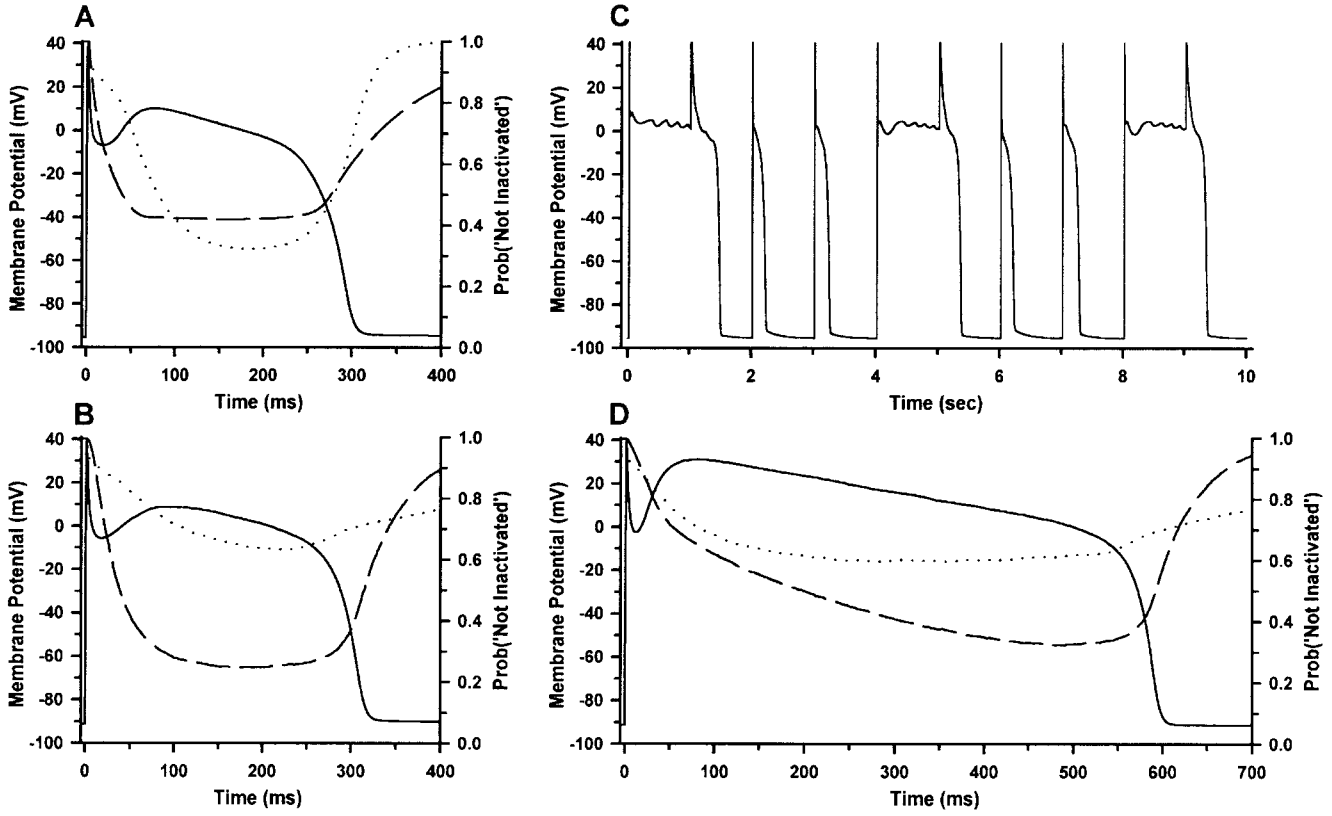

FIGURE 10 Inactivation properties of I_{CaL} in common pool and local control models of the action potential. (*A*) and (*B*), membrane potential (*solid line*, left axis), Prob{*Norm*} (*dashed line*, right axis), and *y* (*dotted line*, right axis) for the Winslow et al. (1999) common pool myocyte model and the local control myocyte model, respectively. Prob{*Norm*} and *y* are the model quantities indicating the time progression of the Ca^{2+}- and voltage-dependent inactivation processes of I_{CaL} (see text for details). (*C*) Membrane potential as a function of time for a 10-s simulation of a modified version of the Winslow et al. (1999) model with I_{CaL} parametrized with strongly Ca^{2+}-dependent and weakly voltage-dependent inactivation (similar to that of the local control model). (*D*) Membrane potential (*solid line*, left axis), Prob{*Norm*} (*dashed line*, right axis), and *y* (*dotted line*, right axis) for the local control myocyte model where SR Ca^{2+} load has been reduced to 33% of its normal level.

common pool and local control models, respectively. Prob{*Norm*} and y are the model quantities indicating the time progression of the Ca^{2+}- and voltage-dependent inactivation processes, respectively, as previously described in Fig. 3 *C*. During the plateau of the AP, ~70% of LCCs become unavailable due to voltage-dependent inactivation while ~60% become unavailable due to Ca^{2+}-dependent inactivation in the common pool model (Fig. 10 *A*). The balance between voltage- and Ca^{2+}-dependent inactivation processes in the Winslow et al. (1999) common pool model are therefore in contrast to experimental findings. The guinea pig models of Jafri et al. (1998) and Luo and Rudy (1994) also exhibit very strong voltage-dependent inactivation of I_{CaL} and relatively weak Ca^{2+}-mediated inactivation (data not shown, see Winslow et al., 2001). The roles of these processes are reversed (as they should be) in the local control myocyte model, with only ~35% of LCCs succumbing to voltage-dependent inactivation, while ~75% are shut down by Ca^{2+}-dependent inactivation (Fig. 10 *B*, compare to Fig. 11 of Linz and Meyer, 1998). Understanding the fundamental differences in the CICR processes in the common pool versus the local control models provides the reason why the balance between each of the inactivation processes is incorrectly assigned in the common pool model. In a model where the release of SR Ca^{2+} is controlled by sensing Ca^{2+} levels in the same pool into which SR Ca^{2+} is released, Ca^{2+} release will be an all-or-none response (Stern, 1992). If Ca^{2+}-dependent inactivation of LCCs were the dominant inactivation process in this type of model, then it follows that I_{CaL} inactivation would also exhibit all-or-none behavior, switching on in response to SR Ca^{2+} release. The single regenerative SR release event would rapidly and strongly promote Ca^{2+}-dependent inactivation of I_{CaL}, and would therefore destabilize the plateau phase of the AP. An attempt at simulating APs using the Winslow et al. (1999) model modified to have strongly Ca^{2+}-dependent and weakly voltage-dependent inactivation of I_{CaL} (with equations governing y identical to that of the local control model) is illustrated in Fig. 10 *C*. APs alternate between those with short duration (~150–250 ms) and those with very long duration (>1000 ms) with unstable oscillatory plateau potentials. The alternans indicate the presence of a bifurcation in the AP profile as a function of JSR Ca^{2+} load. Short-duration APs occur when the all-or-none SR Ca^{2+} release event strongly inactivates I_{CaL}, and hence terminates the AP. SR Ca^{2+} load will be gradually diminished following successive short APs due to the imbalance between cellular Ca^{2+} influx (via LCCs) and Ca^{2+} efflux (via Na^+/Ca^{2+} exchangers and sarcolemmal Ca^{2+} pumps). When the SR becomes sufficiently depleted, the weak SR Ca^{2+} release flux produces only slight inactivation of I_{CaL}. In addition, the population of RyRs fails to adequately inactivate/adapt, leading to additional spontaneous release events and a long-lasting unstable oscillatory plateau. This unstable behavior occurs over a wide range of LCC inactivation parameters as long as voltage-dependent inactivation of I_{CaL} is relatively slow and incomplete (data not shown). Strong voltage-dependent inactivation of I_{CaL}, although contrary to experimental observations, is therefore necessary to enforce stability of those common pool models that incorporate the regenerative SR release mechanisms of CICR. As seen in Fig. 10 *B*, the local control myocyte model does not suffer from the consequences of all-or-none SR Ca^{2+} release (at the whole-cell level) and therefore successfully generates stable APs with LCCs whose inactivation process is dominated by local Ca^{2+}-mediated inactivation.

Altered EC coupling in both human (Lindner et al., 1998) and canine (Hobai and O'Rourke, 2001) heart failure is associated with decreased SR Ca^{2+} content. Both modeling (Winslow et al., 1999) and experimental studies (Ahmmed et al., 2000; O'Rourke et al., 1999) support the idea that altered Ca^{2+} handling plays a key role in heart failure-associated AP prolongation. Fig. 10 *D* shows an AP (*solid line*), Prob{*Norm*} (*dashed line*), and y (*dotted line*) for the local control model under conditions where SR Ca^{2+} load has been reduced to 33% of its normal level. This is a non-steady-state simulation in which the pre-stimulus initial condition for SR Ca^{2+} load (in NSR and all JSR compartments) has been reduced three-fold from control without any alteration in model parameters, thereby isolating the impact of depressed SR Ca^{2+} load on the AP. The voltage-dependent inactivation mechanism proceeds in a manner similar to that of the control case (*dotted line*). However, under conditions of reduced SR Ca^{2+} release, Ca^{2+}-mediated inactivation of I_{CaL} occurs at a far slower rate and to a lesser extent (*dashed line*) than in the control case (compare to Fig. 10 *B*). The resulting increased magnitude of the late sustained component of I_{CaL} (not shown) maintains the plateau and dramatically prolongs the AP (*solid line*). This supports the hypothesis that in heart failure, alterations in Ca^{2+} handling proteins that decrease SR Ca^{2+} load and reduce the amplitude of local Ca^{2+} transients may contribute substantially to prolongation of APD by reducing Ca^{2+}-mediated inactivation of the L-type current.

In a previous study (Greenstein et al., 2000), we examined the role of I_{to1} in shaping AP morphology and duration using the common pool canine myocyte model (Winslow et al., 1999). These simulations predicted that reduction of I_{to1} density from normal levels leads to modest shortening of APD. The reduction in I_{to1} reduces the depth of the phase 1 AP notch, reducing the driving force for, and hence the peak level of, I_{CaL}. Because this study was performed in a model displaying all-or-none rather than graded SR Ca^{2+} release properties, the altered I_{CaL} had no ability to modulate F_{RyR}. In Fig. 11 the role of I_{to1} is revisited, with particular attention to how an alteration of AP shape influences EC coupling. Under normal 1-Hz steady-state conditions (*solid black line*) the AP has a duration of ~315 ms (Fig. 11 *A*), peak I_{CaL} is ~4.8 pA pF^{-1} (Fig. 11 *B*), peak F_{RyR} is ~0.8

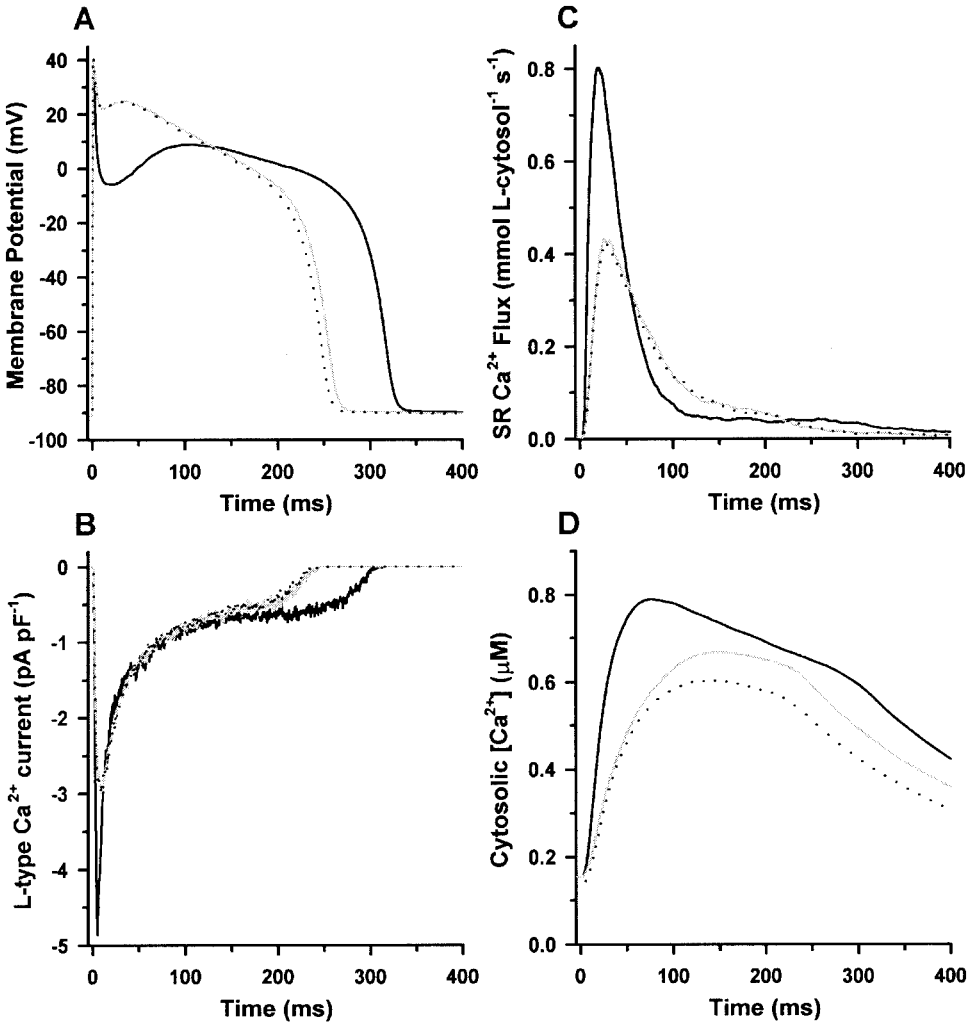

FIGURE 11 Role of I_{to1} on the events of EC coupling. (*A*) Membrane potential, (*B*) L-type Ca^{2+} current (I_{CaL}), (*C*) SR Ca^{2+} release flux (F_{RyR}), and (*D*) cytosolic Ca^{2+} concentration as a function of time. Each of the signals is shown under normal 1-Hz steady-state conditions (*solid black line*), with 67% reduction in I_{to1} density using the normal initial conditions (*gray line*), and with 67% reduction in I_{to1} density under 1-Hz steady-state conditions (see text for details). The altered shape of the AP resulting from reduction in I_{to1} reduces trigger influx Ca^{2+} via LCCs leading to decreased SR Ca^{2+} release flux, and therefore a depressed cytosolic Ca^{2+} transient.

mmol L-cytosol^{-1} s^{-1} (Fig. 11 *C*), and peak cytosolic Ca^{2+} concentration is ~0.8 μM (Fig. 11 *D*). (Note that slight differences in control simulations in Fig. 11 compared to Fig. 9 arise due to stochastic noise inherent in the model.) The density of I_{to1} was then reduced by 67%, an amount similar to that observed in failing canine myocytes (Kääb et al., 1996), and simulations were repeated using normal initial conditions to demonstrate the role of graded SR Ca^{2+} release under conditions of identical SR Ca^{2+} load. The phase 1 notch of the AP becomes less pronounced, and APD is shortened modestly to ~255 ms (Fig. 11 *A, gray line*). The corresponding peak I_{CaL} is reduced by 40% to ~2.9 pA pF^{-1} (Fig. 11 *B*). The property of graded SR Ca^{2+} release is evident by observing F_{RyR} (Fig. 11 *C, gray line*). The reduction in trigger Ca^{2+} reduces peak SR Ca^{2+} release flux by nearly 50% under conditions where SR load is unchanged. The resulting cytosolic Ca^{2+} transient is consequently reduced to ~0.65 μM (Fig. 11 *D*). Although this is a good demonstration of the effects of graded release during the AP, a sudden decrease in I_{to1} is not a physiologically relevant event. Upon pacing to steady state with a 67% reduction of I_{to1} (*dotted line*), both graded SR Ca^{2+} release and the new steady-state SR Ca^{2+} load affect Ca^{2+} cycling properties. The shortening of the APs results in a decreased steady-state SR Ca^{2+} load compared to control (data not shown), which in turn leads to a further decrease in SR Ca^{2+} release, reducing the amplitude of the cytosolic Ca^{2+} transient to ~0.6 μM, 25% less than control (Fig. 11 *D*). The model therefore predicts that reduction in I_{to1}, similar to that observed in heart failure (Kääb et al., 1996), may contribute to reduced force generation. This model prediction has been verified by recent experiments showing that slowed phase 1 repolarization during the AP reduces temporal synchrony and recruitment of Ca^{2+} release events, in conjunction with a reduced amplitude of I_{CaL} (Sah et al., 2002).

DISCUSSION

In this study we present a biophysically detailed model of the normal canine ventricular myocyte that conforms to the theory of local control of EC coupling in cardiac muscle.

Local control theory asserts that L-type Ca^{2+} current tightly controls SR Ca^{2+} release because elementary, independent SR Ca^{2+} release events occur in response to highly localized Ca^{2+} transients, which are produced by the opening of single L-type Ca^{2+} channels in the vicinity of a small cluster of RyRs (Stern, 1992; Bers, 1993; Wier et al., 1994; Sham et al., 1995). Tight regulation of CICR is made possible by the fact that LCCs and RyRs are sensitive to local submembrane Ca^{2+}, rather than global Ca^{2+} levels, allowing for graded control of Ca^{2+} release while maintaining high EC coupling gain (Fabiato, 1985; Beuckelmann and Wier, 1988; Sham, 1997). To capture these properties of local control, our myocyte model incorporates EC coupling in the form of Ca^{2+} release units in which individual sarcolemmal L-type Ca^{2+} channels interact in a stochastic manner with nearby RyRs in localized regions where junctional SR membrane and T-tubular membrane are in close proximity. The CaRUs are embedded within and interact with the global systems of the myocyte describing ionic and membrane pump/exchanger currents, SR Ca^{2+} uptake, and time-varying cytosolic ion concentrations. The results demonstrate that a single comprehensive model of the cardiac myocyte can reproduce both detailed properties of EC coupling predicted by local control theory, such as variable gain and graded SR Ca^{2+} release, while at the same time reproducing whole-cell phenomena, such as modulation of AP duration by SR Ca^{2+} release. The ability of this model to encompass mechanisms of both microscopic and macroscopic phenomena afford it the unique ability to provide insight into the integrative properties of the myocyte that arise from the interaction among these subcellular processes.

The main goal of this study was to develop a myocyte model incorporating mechanistic descriptions of the processes that underlie local control of SR Ca^{2+} release. This requires the simulation of a large number of individual stochastically gating channels, which poses a substantial computational task. To maintain tractability, the CaRU was designed as a "minimal model," including biophysically detailed descriptions of individual LCCs and RyRs (Jafri et al., 1998; Rice et al., 1999; Keizer and Smith, 1998). Each CaRU contains four subspace compartments in which elementary Ca^{2+} release events may occur, allowing for passive flow of Ca^{2+} to neighboring subspaces providing for the possibility that an initial release event may trigger an additional release event in the neighboring cluster of RyRs (Parker et al., 1996; Song et al., 2001). This geometry allows the summation of release events within a CaRU to serve as a minimal model of a Ca^{2+} spike while reproducing fundamental properties of EC coupling measured at the whole cell level, such as graded Ca^{2+} release. It is important to note, however, that the individual release events within the CaRU are not intended to reproduce the detailed spatiotemporal properties of experimentally observed Ca^{2+} sparks (Fig. 4 *A*) (Cheng et al., 1993). Such a model would require explicit descriptions of dyadic subspace geometry, Ca^{2+} diffusion, and surface charge effects. Models accounting for these features have been developed for a single isolated dyad (Cannell and Soeller, 1997; Soeller and Cannell, 1997; Langer and Peskoff, 1996), but would be too computationally demanding for this application.

Stern et al. (1999) have demonstrated that a number of RyR models, with rate constants determined from measurements in lipid bilayers (Zahradnikova and Zahradnik, 1996; Keizer and Levine, 1996; Schiefer et al., 1995) exhibit local instability (failure of SR release termination following activation) or global instability (spontaneous activation by background Ca^{2+}) when simulated in a local control environment. Furthermore, they have shown that stability of local control requires that RyRs exhibit strong inactivation and cooperative activation by more than one Ca^{2+} ion, and have suggested that such properties may arise from allosteric interactions between neighboring RyRs. The RyR model formulation presented in this study, which is based on that of Keizer and Smith (1998), exhibits both strong inactivation/adaptation properties consistent with rates observed in the presence of Mg^{2+} (Valdivia et al., 1995), and requires cooperative binding of four Ca^{2+} ions in order to open. Although there is mounting evidence that RyR gating properties are influenced by physical coupling of neighboring RyRs (Marx et al., 2001), the results of this study suggest that the stability of local control of SR Ca^{2+} release can be achieved without accounting for such interactions explicitly.

The local control myocyte model description requires that I_{CaL} be computed based on the ensemble behavior of individually simulated LCCs. This requires that both single channel properties (e.g., unitary conductance, open and closed time distributions) and whole-cell current properties (e.g., peak current-voltage relation, steady-state inactivation) are incorporated into the model, unlike typical macroscopic model formulations that need only describe whole-cell properties. Figs. 2 and 3 demonstrate that the LCC model reproduces both single channel (Herzig et al., 1993; Handrock et al., 1998; Schroder et al., 1998; Rose et al., 1992; Yue and Marban, 1990) and whole-cell (Hobai and O'Rourke, 2001; Kääb et al., 1996; O'Rourke et al., 1999; Rose et al., 1992; He et al., 2001; Linz and Meyer, 1998; Sipido et al., 1995; Sham, 1997; Hadley and Hume, 1987; Peterson et al., 1999; Li et al., 1999) current properties rather well. A model based prediction of ~50,000 was obtained for N_{active}, the number of active (phosphorylated) LCCs in a cardiac myocyte, which agrees well with experimental estimates (Rose et al., 1992; McDonald et al., 1986). In keeping with the approach of a "minimal model," only active LCCs were simulated and the process of slow cycling between active and silent modes of behavior (Herzig et al., 1993) was not included in the model.

The I_{CaL} steady-state inactivation curve (Fig. 3 *D*) demonstrates how whole-cell properties emerge from mechanis-

tic descriptions of underlying processes. The model steady-state inactivation curve is U-shaped under normal conditions, but monotonically decreases and is incomplete with increasing membrane potential when Ca^{2+} is not the charge carrier, which agrees well with experiments (Hadley and Hume, 1987; Linz and Meyer, 1998; Li et al., 1999). Some previous models of I_{CaL} have been able to reproduce the phenomena of U-shaped inactivation by incorporating this property directly into the equations describing inactivation (Jafri et al., 1998; Sun et al., 2000). In the local control myocyte model, however, the U-shaped inactivation curve emerges as a consequence of local Ca^{2+}-mediated events. The magnitude of the local Ca^{2+} transient is graded as a function of LCC Ca^{2+} influx, which is maximal in the central range of potentials of −10 mV to +30 mV (Fig. 3 *B*). The local rise in Ca^{2+} induces Ca^{2+}-mediated inactivation of I_{CaL}, which makes a dominant contribution to the total inactivation of I_{CaL} when local Ca^{2+} levels are raised (e.g., Fig. 3 *C*). The U-shape therefore emerges as a reflection of the bell-shaped voltage dependence of LCC Ca^{2+} influx.

By summing over all of the local events that occur in the CaRUs, model simulations are able to faithfully reproduce details regarding the relationship between whole-cell I_{CaL} and whole-cell SR Ca^{2+} release. In response to a depolarizing voltage clamp pulse, the whole-cell SR Ca^{2+} release flux peaks soon after depolarization and then decays to a small maintained component in a similar manner to signals measured experimentally (Wier et al., 1994). The small amplitude maintained release is supported by the slow/sustained component of I_{CaL} and turns off following repolarization to the resting potential (Fig. 5 *A*). Control of SR Ca^{2+} release by I_{CaL} has been demonstrated experimentally by showing that SR Ca^{2+} release can be turned off by termination of Ca^{2+} current (Wier et al., 1994; Cannell et al., 1987; Cleemann and Morad, 1991). Although the SR Ca^{2+} release flux in response to a short-duration pulse has not been shown explicitly in this study, the model does exhibit this behavior. The exemplar Ca^{2+} spike shown in Fig. 4 *C* occurred ~25 ms following the onset of the depolarizing voltage clamp pulse, and clearly would not have been triggered if the pulse was truncated to $\ll$25 ms. Additional evidence for control of SR Ca^{2+} release by I_{CaL} has been demonstrated by the ability of I_{CaL} tail currents, occurring upon repolarization to the rest potential following a depolarized voltage clamp, to trigger a release event (Wier et al., 1994; Sham et al., 1998). The local control model readily reproduces this response (Fig. 8, *B* and *D*). Upon membrane depolarization, the model demonstrates that the mean dyadic subspace Ca^{2+} concentration reaches levels that are >20-fold greater than in the cytosol (Fig. 5 *B*), consistent with both experimental and theoretical predictions that submembrane Ca^{2+} can reach concentrations that are much higher than in the cytosol (Sham, 1997; Stern, 1992; Langer and Peskoff, 1996; Soeller and Cannell, 1997; Jafri et al., 1998; Cheng et al., 1993; Wang et al., 2001; Song et al., 2001). It has been noted recently that the common pool model of Winslow et al. (1999) has a limitation in that the SR is almost two-thirds depleted upon a single stimulus (Michailova and McCulloch, 2001). The local control model of this study demonstrates both fractional SR release (~32%) and total pre-release SR Ca^{2+} content (~118 μmol L-cytosol^{-1}) consistent with experimental studies (Bassani et al., 1995; DelBridge et al., 1996; Hobai and O'Rourke, 2001).

The key experimental observation that has suggested the process of CICR is locally controlled is that while both $F_{RyR(max)}$ and $F_{LCC(max)}$ exhibit a bell-shaped dependence on membrane potential, the relationships are not the same (Wier et al., 1994; Santana et al., 1996; Cannell et al., 1995; Janczewski et al., 1995; Wier and Balke, 1999). At negative potentials, single channel currents are large, but macroscopic current is relatively small due to the fact that LCC openings are infrequent. This implies that LCC openings are sparsely dispersed throughout the membrane. As a result, I_{CaL} in this potential range is more effective at triggering SR Ca^{2+} release than at positive potentials, where single channel openings are far more frequent but unitary current magnitude is smaller. This behavior reveals itself in the model in the form of a shift in the voltage dependence of $F_{RyR(max)}$ vs. $F_{LCC(max)}$ (Fig. 7 *B*) and in the form of graded SR Ca^{2+} release with variable EC coupling gain that decreases with increasing membrane potential (Fig. 7 *C*) similar to curves obtained experimentally (Wier et al., 1994; Santana et al., 1996; Cannell et al., 1995; Janczewski et al., 1995) and theoretically (Stern, 1992; Stern et al., 1999). Gain decreases with increasing depolarization due to the decrease in local triggering efficiency that occurs as unitary current magnitude decreases. Experimentally measured EC coupling gain functions typically display a steeper slope at negative potentials compared to positive potentials (Wier et al., 1994; Song et al., 2001). Simulations using the local control myocyte model show that coupling among neighboring subspace compartments within the CaRUs is necessary to generate responses with relatively very high gain at the most negative potentials (Fig. 7 *C, triangles*). At negative voltages, where the unitary current magnitude is relatively high, the Ca^{2+} influx from the opening of a single LCC is sufficient to trigger SR release from RyRs that reside in the same dyadic subspace compartment, as well as from RyRs in adjacent subspace compartments, but within the same T-SR junction (i.e., the same CaRU). The number of RyRs that may sense trigger Ca^{2+} from a particular LCC is effectively increased with increasing unitary LCC current, increasing the slope of the gain function at negative potentials. The simulated EC coupling gain function, however, falls somewhat short of the values measures experimentally at negative voltages (e.g., at −30 mV: model gain, ~28; Wier et al., 1994, >40; Song et al., 2001, ~42). This discrepancy in slope of the gain function at negative poten-

tials results from the "minimal model" assumption that a single LCC can trigger activity of no more than 20 RyRs (i.e., only the RyRs within a single CaRU) regardless of the strength of inter-subspace coupling. As described above, the choice of only four subunits per CaRU was necessary to retain minimal model complexity in the description of local Ca^{2+} diffusion. Model EC coupling gain at negative voltages would be increased in line with experimental data if the dyad of each CaRU were expanded from our minimal representation to include a greater number of LCC-RyR functional groupings (~100 RyRs per dyad) as has been observed in structural studies (Franzini-Armstrong et al., 1999).

The fact that SR Ca^{2+} release is graded is a property that emerges from considering the mechanistic details of local interactions between LCCs and RyRs. Our myocyte model is not the first to exhibit SR Ca^{2+} release that is graded. Previous myocyte models (Luo and Rudy, 1994; Faber and Rudy, 2000; Fox et al., 2002), however, achieved the graded SR release phenomenologically by formulating SR Ca^{2+} release flux as a direct function of sarcolemmal Ca^{2+} influx rather than a function of Ca^{2+} concentration at the site of the RyRs. Even though these formulations are capable of generating graded CICR, a formulation of SR Ca^{2+} release that depends only upon macroscopic Ca^{2+} influx cannot reproduce an EC coupling gain function that decreases monotonically with increasing membrane potential (Fig. 7 *C*).

Many cardiac Ca^{2+} cycling proteins that play a role in EC coupling, including LCCs (Herzig et al., 1993; Handrock et al., 1998) and RyRs (Marx et al., 2000), are known target proteins of the β-adrenergic receptor (β-AR)-adenylyl cyclase-cAMP-protein kinase A signaling pathway. An increase in β-adrenergic stimulation, such as that which occurs during heart failure (Handrock et al., 1998; Marx et al., 2000), tends to increase channel availability or promote faster kinetics. The microscopic mechanisms underlying β-AR-mediated modulation of EC coupling are not well understood. Recent experiments suggest that improved synchronization of SR Ca^{2+} release both within and among T-SR junctions, and hence increased cardiac inotropy, occurs as a result of increased β-adrenergic stimulation (Song et al., 2001). In this study, it has been demonstrated that baseline model Ca^{2+} spike statistics, both within and among CaRUs, agree well with those measured in experiments (Fig. 6) (Song et al., 2001). Additional experiments have demonstrated that heart failure-related alterations in LCC properties might not be apparent in whole-cell I_{CaL} measurements. Single LCCs from failing human ventricular myocytes exhibit increased availability and open probability compared to nonfailing myocytes, while whole-cell current measurements do not reveal a change in I_{CaL} current density, suggesting that the number of functional channels must be reduced in failing myocytes (Schroder et al., 1998). In failing canine myocytes, the number of LCCs has been found to be reduced as well via measurement of intramembrane charge movement, where whole-cell currents were again found to be unchanged (He et al., 2001). In failing hearts, RyRs have been found to be hyperphosphorylated, leading to dissociation of FKBP12.6 regulatory subunits, which results in both increased Ca^{2+} sensitivity for activation and elevated channel open probability (Marx et al., 2000). Macroscopically defined myocyte models do not account for single channel properties, and are not useful in interpreting these findings. The local control myocyte model, however, provides a means to study detailed mechanisms of β-AR-mediated and/or heart failure-related alterations in LCC, RyR, and Ca^{2+} spike properties, and the role such alterations would have on both microscopic EC coupling and whole-cell behavior.

It is widely accepted that I_{CaL} inactivates via both voltage-dependent and Ca^{2+}-mediated processes. Recent experiments have elucidated mechanistic details of the Ca^{2+}-mediated inactivation process, indicating that calmodulin is tethered to the LCC and acts as a critical Ca^{2+} sensor, and that targeted mutations that prevent calmodulin binding to the LCC (Zuhlke et al., 1999) or prevent Ca^{2+} binding to calmodulin (Peterson et al., 1999, 2000), dramatically reduce the degree of I_{CaL} inactivation observed during a depolarizing voltage clamp pulse. It has also been shown that Ca^{2+}-mediated inactivation plays a dominant role in I_{CaL} inactivation under AP clamp protocols (Linz and Meyer, 1998) and under voltage clamp protocols where SR Ca^{2+} load is varied (Sipido et al., 1995; Sham, 1997). Although experimental evidence indicates that the Ca^{2+}-mediated inactivation process is dominant and the voltage-dependent process is far slower, mathematical models of I_{CaL} have consistently been formulated with strong voltage-dependent inactivation and relatively weaker Ca^{2+}-mediated inactivation (Winslow et al., 1999; Jafri et al., 1998; Luo and Rudy, 1994; Pandit et al., 2001). The local control myocyte model presented in this study displays strong Ca^{2+}-mediated LCC inactivation properties consistent with experimental findings (Figs. 3 *D* and 10 *B*). Moreover, Fig. 10 demonstrates that the all-or-none SR Ca^{2+} release property of common pool models (with explicit descriptions of CICR mechanisms) precludes stability of simulated APs when the balance between Ca^{2+}-mediated and voltage-dependent inactivation of I_{CaL} is adjusted to be consistent with experimental findings. This points to a critical flaw of these common pool model formulations for Ca^{2+} cycling within the cardiac myocyte. In a number of animal models of heart failure, EC, coupling processes have been found to be defective (Lindner et al., 1998; Hobai and O'Rourke, 2001; Ahmmed et al., 2000; Marx et al., 2000; Schroder et al., 1998; He et al., 2001; Gomez et al., 1997; O'Rourke et al., 1999). A clear and quantitative understanding of Ca^{2+} cycling and the microscopic details of CICR are critical to the elucidation of heart failure-related alterations in EC coupling. It may be difficult to interpret altered EC coupling

TABLE 1 Physical constants and cell geometry parameters

Parameter	Definition	Value
F	Faraday constant	96.5 C $mmol^{-1}$
T	Absolute temperature	310 K
R	Universal gas constant	8.314 J mol^{-1} K^{-1}
C_{SA}	Cell surface area capacitance	153.4 pF
V_{cyto}	Cytosolic volume	25.84 pL
V_{NSR}	NSR volume	1.113 pL
V_{JSR}	JSR volume (single compartment)	22.26×10^{-6} pL
V_{SS}	SS volume (single compartment)	0.203×10^{-6} pL
N_{CaRU}	Number of Ca^{2+} release units	12,500

TABLE 2 Standard ionic concentrations

Parameter	Definition	Value (mM)
$[K^+]_o$	Extracellular K^+ concentration	4.0
$[Na^+]_o$	Extracellular Na^+ concentration	138.0
$[Ca^{2+}]_o$	Extracellular Ca^{2+} concentration	2.0
$[Cl^-]_o$	Extracellular Cl^- concentration	150.0
$[Cl^-]_{cyto}$	Intracellular Cl^- concentration	20.0

processes in the context of a common pool model due to the inherent instability of I_{CaL} in that environment. The local control myocyte model, however, displays robust graded SR Ca^{2+} release and strong Ca^{2+}-mediated inactivation of I_{CaL}, processes that are central to properties of CICR. As an example, the model demonstrates that depressed SR Ca^{2+} content similar to that measured in heart failure (Lindner et al., 1998; Hobai and O'Rourke, 2001) leads to dramatic AP prolongation by relieving the strong Ca^{2+}-mediated inactivation of LCCs (Fig. 10 *D*). In addition, the coupling of quantitative descriptions of microscopic events of CICR to the macroscopic processes within the myocyte reveals how the integration of these cellular processes gives rise to phenomena that may be difficult to predict or understand without interpretation in the context of a quantitative model (Fig. 11).

The local control myocyte model provides a means for studying the interrelationship between microscopic and macroscopic behaviors in a manner that would not be possible in experiments. It is likely that the role of local stochastic interactions in determining macroscopic properties applies to physiological systems other than CICR in cardiac myocytes. In a model of phage λ-infection (Arkin et al., 1998), molecular level fluctuations in the rates of gene expression can arise due to stochastic local actions of regulatory proteins. These fluctuations lead to highly erratic time patterns of protein production in individual cells, which determine the phenotypic outcome for the phage λ lysis-lysogeny decision circuit. Recordings from rat hippocampal neurons have demonstrated the existence of a preassembled macromolecular signaling complex, which associates the β-AR with the L-type Ca^{2+} channel (Davare et al., 2001). The complex also contains a G-protein, an adenylyl cyclase, protein kinase A, and a phosphatase. The physical association of the molecular components of these signaling pathway elements suggests that the chain of signaling events from receptor-ligand binding to phosphorylation of the LCC will be determined by interactions between a small number of molecular entities within their local environment. Modeling studies of systems such as these may benefit from an approach, such as the one presented in

TABLE 4 Ryanodine receptor parameters

Parameter	Definition	Value
k_{12}	Rate constant: state 1 to state 2	877.5 mM^{-2} ms^{-1}
k_{21}	Rate constant: state 2 to state 1	250.0 ms^{-1}
k_{23}	Rate constant: state 2 to state 3	2.358×10^8 mM^{-2} ms^{-1}
k_{32}	Rate constant: state 3 to state 2	9.6 ms^{-1}
k_{34}	Rate constant: state 3 to state 4	1.415×10^6 mM^{-2} ms^{-1}
k_{43}	Rate constant: state 4 to state 3	13.65 ms^{-1}
k_{45}	Rate constant: state 4 to state 5	0.07 ms^{-1}
k_{54}	Rate constant: state 5 to state 4	93.385 mM^{-2} ms^{-1}
k_{56}	Rate constant: state 5 to state 6	1.887×10^7 mM^{-2} ms^{-1}
k_{65}	Rate constant: state 6 to state 5	30.0 ms^{-1}
k_{25}	Rate constant: state 2 to state 5	2.358×10^6 mM^{-2} ms^{-1}
k_{52}	Rate constant: state 5 to state 2	0.001235 ms^{-1}
r_{RyR}	Rate of Ca^{2+} flux through an open RyR	3.92 ms^{-1}

TABLE 3 L-type Ca^{2+} channel and Ca^{2+}-dependent Cl^- channel parameters

Parameter	Definition	Value
f	LCC transition rate into open state	0.85 ms^{-1}
g	LCC transition rate out of open state	2.0 ms^{-1}
f'	LCC transition rate into open state for Mode Ca	0.005 ms^{-1}
g'	LCC transition rate out of open state for Mode Ca	7.0 ms^{-1}
a	LCC mode transition parameter	2.0
b	LCC mode transition parameter	1.9356
γ_o	LCC mode transition parameter	0.44 mM^{-1} ms^{-1}
ω	LCC mode transition parameter	0.02158 ms^{-1}
P_{CaL}	L-type Ca^{2+} channel permeability to Ca^{2+} (unitary)	9.13×10^{-13} cm^3 s^{-1}
$K_{d,ClCh}$	Dissociation constant of ClCh for Ca^{2+}	0.1502 mM
$k_{f,ClCh}$	ClCh transition rate into open state ($k_{b,ClCh}/K_{d,ClCh}$)	13.3156 mM^{-1} ms^{-1}
$k_{b,ClCh}$	ClCh transition rate out of open state	2.0 ms^{-1}
P_{to2}	Ca^{2+}-dependent Cl^- channel permeability to Cl^- (unitary)	2.65×10^{-15} cm^3 s^{-1}

TABLE 5 Ca^{2+} flux and buffering parameters

Parameter	Definition	Value
r_{xfer}	Rate of Ca^{2+} flux between SS and cytosol	200.0 ms^{-1}
r_{tr}	Rate of Ca^{2+} flux between NSR and JSR	0.333 ms^{-1}
r_{iss}	Intersubspace Ca^{2+} flux rate	20.0 ms^{-1}
$[BSR]_T$	Total subspace SR membrane site concentration	47.0 μM
K_{BSR}	Ca^{2+}-half-saturation constant for BSR	0.87 μM
$[BSL]_T$	Total subspace sarcolemma site concentration	1124.0 μM
K_{BSL}	Ca^{2+}-half-saturation constant for BSL	8.7 μM
$[CSQN]_T$	Total JSR calsequestrin concentration	13.5 mM
K_{CSQN}	Ca^{2+}-half-saturation constant for calsequestrin	0.63 mM
$[CMDN]_T$	Total cytosolic calmodulin concentration	50.0 μM
K_{CMDN}	Ca^{2+}-half-saturation constant for calmodulin	2.38 μM

this study, which combines stochastic and deterministic methods to maintain detailed descriptions of local molecular interactions. Furthermore, the need for implementing local molecular interactions poses a unique challenge to the scientific community. More mathematically efficient ways of describing local phenomena are necessary to build models that can be used to rapidly explore hypotheses and/or can be incorporated into larger-scale multicellular tissue or whole organ models.

APPENDIX I

Local ionic fluxes

Each Ca^{2+} release unit (CaRU) contains a single JSR compartment and four dyadic subspace compartments, which are arranged on a 2 × 2 grid (Fig. 1). Between each subspace and the JSR compartment there are five RyRs, and between each subspace and the T-tubule lumen there is one LCC and one ClCh. All model parameter values are given in Tables 1–7.

The JSR volume of the *i*th CaRU is refilled via passive Ca^{2+} influx from the NSR:

$$J_{tr,i} = r_{tr}([Ca^{2+}]_{NSR} - [Ca^{2+}]_{JSR,i}) \quad (1)$$

where r_{tr} is the transfer rate of Ca^{2+} from the NSR to a JSR compartment; $[Ca^{2+}]_{NSR}$ is the NSR Ca^{2+} concentration; and $[Ca^{2+}]_{JSR,i}$ is the JSR Ca^{2+} concentration in the *i*th CaRU. Total Ca^{2+} flux from NSR into all CaRU JSR compartments is

$$J_{tr} = \frac{N_{CaRU}}{N_s} \sum_{i=1}^{N_s} J_{tr,i} \quad (2)$$

where N_{CaRU} is the number of CaRUs included in the full model and N_s is the number of CaRUs actually simulated (see Appendix II for description of N_{CaRU} vs. N_s). Diffusive Ca^{2+} flux between the *j*th and the *l*th contiguous subspaces within the *i*th CaRU is defined by

$$J_{iss,i,j,l} = r_{iss}([Ca^{2+}]_{SS,i,j} - [Ca^{2+}]_{SS,i,l}) \quad (3)$$

where r_{iss} is the inter-subspace Ca^{2+} transfer rate and $[Ca^{2+}]_{SS,i,j}$ is the subspace Ca^{2+} concentration in the *j*th subspace of the *i*th CaRU. Every subspace compartment has two neighbors into which or from which Ca^{2+} may flow (Fig. 1 *B*). Similarly, Ca^{2+} diffusion out of the *j*th subspace of the *i*th CaRU into the cytosol is calculated as

$$J_{xfer,i,j} = r_{xfer}([Ca^{2+}]_{SS,i,j} - [Ca^{2+}]_{cyto}) \quad (4)$$

where r_{xfer} is the rate of Ca^{2+} transfer from a single subspace compartment to the cytosol and $[Ca^{2+}]_{cyto}$ is the cytosolic Ca^{2+} concentration. The total Ca^{2+} flux entering the cytosol from all CaRUs is

$$J_{xfer} = \frac{N_{CaRU}}{N_s} \sum_{i=1}^{N_s} \sum_{j=1}^{4} J_{xfer,i,j} \quad (5)$$

The Markov state model for the L-type Ca^{2+} channel is the mode-switching model developed previously by Jafri et al. (1998) and is shown in Fig. 12 *A*. Briefly, the upper row of states comprises Mode Normal, while the lower row of states comprises Mode Ca, the Ca^{2+}-mediated inactivation mode. States labeled *O* and O_{Ca} (states 6 and 12) are conducting states. Elevation of local Ca^{2+} level promotes transition into Mode Ca, in which transitions to the open state are extremely rare. The rate constants are defined individually for each LCC by the parameter values given in Table 3 and

TABLE 6 Ionic current and flux formulations from previous studies

Current/Flux	Reference	New Parameter Values
Fast Na^+ current (I_{Na})	Winslow et al., 1999	No change
Rapid delayed rectifier K^+ current (I_{Kr})	Mazhari et al., 2001	G_{Kr} = 0.024 mS μF^{-1}
Slow delayed rectifier K^+ current (I_{Ks})	Winslow et al., 1999	No change
Transient outward K^+ current (I_{to1})	Greenstein et al., 2000	$G_{Kv4.3}$ = 0.1389 mS μF^{-1} $P_{Kv1.4}$ = 1.989 × 10^{-7} cm s^{-1}
Time-independent K^+ current (I_{K1})	Winslow et al., 1999	G_{K1} = 3.0 mS μF^{-1}
Plateau K^+ current (I_{Kp})	Winslow et al., 1999	G_{Kp} = 0.002659 mS μF^{-1}
Na^+/Ca^{2+} exchanger current (I_{NaCa})	Winslow et al., 1999	k_{NaCa} = 0.27 pA pF^{-1}
Na^+/K^+ pump current (I_{NaK})	Winslow et al., 1999	$I_{NaK,max}$ = 0.901 pA pF^{-1}
Sarcolemmal Ca^{2+} pump current ($I_{p(Ca)}$)	Winslow et al., 1999	$I_{p(Ca),max}$ = 0.03 pA pF^{-1} $K_{m,p(Ca)}$ = 0.0005 mM
Ca^{2+} background current ($I_{Ca,b}$)	Winslow et al., 1999	$G_{Ca,b}$ = 0.0002536 mS μF^{-1}
Na^+ background current ($I_{Na,b}$)	Winslow et al., 1999	$G_{Na,b}$ = 0.00264 mS μF^{-1}
Ca^{2+} binding to troponin (J_{trpn})	Winslow et al., 1999	No change
SR Ca^{2+} pump (SERCA2a pump, J_{up})	Shannon et al., 2000	V_{maxf} = V_{maxr} = 209.6 μM s^{-1}
(Ca^{2+} flux between cytosol and NSR)		k = 0 (leak term omitted)

$$\alpha = 2.0e^{0.012(V_m-35)} \quad (6)$$

$$\beta = 0.0882e^{-0.05(V_m-35)} \quad (7)$$

$$\alpha' = a\alpha \quad (8)$$

$$\beta' = \beta/b \quad (9)$$

$$\gamma = \gamma_o[Ca^{2+}]_{SS} \quad (10)$$

where V_m is membrane potential in units of mV; α, β, α', β', and γ are in units of ms^{-1}; and $[Ca^{2+}]_{SS}$ is the Ca^{2+} concentration in the dyadic subspace adjacent to the inner pore of the channel. Voltage-dependent inactivation of an LCC, indicated by the value of $y_{i,j}$, is modeled by the simple two-state gating scheme shown in Fig. 12 *B*, with rates determined by

$$y_\infty = 0.4/(1 + e^{(V_m+12.5)/5}) + 0.6 \quad (11)$$

$$\tau_y = 340/(1 + e^{(V_m+30)/12}) + 60 \quad (12)$$

$$k_{b,y} = y_\infty/\tau_y \quad (13)$$

$$k_{b,y} = (1 - y_\infty)/\tau_y \quad (14)$$

with τ_y given in ms, and $k_{i,y}$ and $k_{b,y}$ given in ms^{-1}. The current passing through the *j*th LCC of the *i*th CaRU can then be written as

$$I_{LCC,i,j} = \text{isopen}(LCC_{i,j}, y_{i,j})P_{CaL} \times \frac{4V_mF^2}{RT}\frac{[Ca^{2+}]_{SS,i,j}\,e^{2V_mF/RT} - 0.341[Ca^{2+}]_o}{e^{2V_mF/RT} - 1} \quad (15)$$

where isopen($LCC_{i,j}$, $y_{i,j}$) indicates when the *j*th channel of the *i*th CaRU is open and takes on the value of 1 when it occupies state O or O_{Ca}, and is not voltage-inactivated (i.e., $LCC_{i,j}$ is in state 6 or 12 and y_{ij} is in state 1), and takes on the value of 0 otherwise; P_{CaL} is the permeability of a single LCC; F is Faraday's constant; R is the universal gas constant; T is absolute temperature; $[Ca^{2+}]_{SS,i,j}$ is the subspace Ca^{2+} concentration adjacent to the *j*th channel of the *i*th CaRU; and $[Ca^{2+}]_o$ is extracellular Ca^{2+} concentration. Whole-cell I_{CaL}, normalized by whole-cell capacitance, is equal to the summation of unitary Ca^{2+} currents over all LCCs

$$I_{CaL} = \frac{1}{C_{SA}}\frac{N_{CaRU}}{N_s}\sum_{i=1}^{N_s}\sum_{j=1}^{4} I_{LCC,i,j} \quad (16)$$

where C_{SA} is the capacitance of the cell's surface area and it has been assumed that specific membrane capacity is 1 $\mu F\ cm^{-2}$.

The Ca^{2+}-dependent Cl^- channel (ClCh) is modeled as a voltage- and time-independent ligand-gated channel, using a simple two-state model as shown in Fig. 12 *C*. Although detailed Ca^{2+}-dependent kinetics have not been experimentally measured for this channel, model rates have been chosen to be sufficiently fast ($\sim$2 ms^{-1}) to track kinetics of local Ca^{2+} transients, and to be consistent with the experimentally estimated K_d value for Ca^{2+} binding of $\sim$150 μM (Collier et al., 1996). Unitary $C1^-$ current through the *j*th ClCh of the *i*th CaRU is described as

$$I_{ClCh,i,j} = \text{isopen}(ClCh_{i,j})P_{to2} \times \frac{V_mF^2}{RT}\frac{[Cl^-]_{cyto}\,e^{-V_mF/RT} - [Cl^-]_o}{e^{-V_mF/RT} - 1} \quad (17)$$

where isopen($ClCh_{i,j}$) indicates when the *j*th channel of the *i*th CaRU is open and P_{to2} is the permeability of a single ClCh. ClCh permeability is adjusted to match unitary $C1^-$ currents measured in canine ventricular myocytes (Collier et al., 1996). Because other Cl^- transport mechanisms are not included in the model, it was assumed that intracellular/subspace Cl^- concentration remains constant. Whole-cell I_{to2}, normalized by cell

TABLE 7 State variable initial conditions

Variable	Initial Value (Voltage Clamp)*	Initial Value (AP)†
V_m	−100.0 mV	−91.3258 mV
m (I_{Na})	1.21087×10^{-4}	5.33837×10^{-4}
h (I_{Na})	0.999484	0.996345
j (I_{Na})	0.999480	0.997315
$[Na^+]_{cyto}$	10.0 mM	10.0 mM
$[K^+]_{cyto}$	133.24 mM	131.84 mM
$[Ca^{2+}]_{cyto}$	1.11074×10^{-4} mM	1.45273×10^{-4} mM
$[Ca^{2+}]_{NSR}$	0.728737 mM	0.908882 mM
[LTRPNCa]	7.02394×10^{-3} mM	8.98282×10^{-3} mM
[HTRPNCa]	0.136915 mM	0.137617 mM
x_{Ks} (I_{Ks})	0.104829×10^{-3}	0.204717×10^{-3}
C_1 (I_{Kr})	0.990	0.999503
C_2 (I_{Kr})	0.008	0.413720×10^{-3}
C_3 (I_{Kr})	0.002	0.727568×10^{-4}
O (I_{Kr})	0.0	0.873984×10^{-5}
I (I_{Kr})	0.0	0.136159×10^{-5}
C_0 ($I_{Kv4.3}$)	0.968277	0.953060
C_1 ($I_{Kv4.3}$)	0.0133601	0.0253906
C_2 ($I_{Kv4.3}$)	0.691875×10^{-4}	0.253848×10^{-3}
C_3 ($I_{Kv4.3}$)	0.159092×10^{-6}	0.112796×10^{-5}
O ($I_{Kv4.3}$)	0.0	0.187950×10^{-8}
CI_0 ($I_{Kv4.3}$)	0.0153235	0.0151370
CI_1 ($I_{Kv4.3}$)	0.00271424	0.00517622
CI_2 ($I_{Kv4.3}$)	0.243515×10^{-3}	0.896600×10^{-3}
CI_3 ($I_{Kv4.3}$)	0.115007×10^{-4}	0.817569×10^{-4}
OI ($I_{Kv4.3}$)	0.163239×10^{-6}	0.224032×10^{-5}
C_0 ($I_{Kv1.4}$)	0.824239	0.722328
C_1 ($I_{Kv1.4}$)	0.0522865	0.101971
C_2 ($I_{Kv1.4}$)	0.00124396	0.00539932
C_3 ($I_{Kv1.4}$)	0.131359×10^{-4}	0.127081×10^{-3}
O ($I_{Kv1.4}$)	0.522383×10^{-7}	0.182742×10^{-5}
CI_0 ($I_{Kv1.4}$)	0.118010	0.152769
CI_1 ($I_{Kv1.4}$)	0.00334011	0.00962328
CI_2 ($I_{Kv1.4}$)	0.684631×10^{-3}	0.00439043
CI_3 ($I_{Kv1.4}$)	0.136717×10^{-3}	0.00195348
OI ($I_{Kv1.4}$)	0.451249×10^{-4}	0.00143629
$[Ca^{2+}]_{JSR,i}$	0.728921 mM (100%)	0.908408 mM (100%)
$[Ca^{2+}]_{SS,i,j}$	0.111074×10^{-3} mM (100%)	0.145370×10^{-3} mM (100%)
$LCC_{i,j}$	state 1 (100%)	states 1, 2, 7 (95.8%, 3.8%, 0.4%)
$y_{i,j}$	state 1 (100%)	states 0, 1 (94.25%, 5.75%)
$ClCh_{i,j}$	state 0 (100%)	states 0, 1 (99.8%, 0.2%)
$RyR_{i,j,k}$	state 1 (100%)	states 1, 5–6 (60.9%, 39.1%)

For global state variable definitions, see text and references given in Table 6. For CaRU-compartment and CaRU-random state variable definitions, the initial distribution is given in parentheses for each state respectively.
*Initial values for voltage clamp simulations (Figs. 2–8) correspond to the state of the system after holding at −100 mV for $\sim$3 s following a train of 200-ms voltage clamp pulses to 0 mV applied at 1 Hz (to load SR with Ca^{2+}).
†Initial values for APs (Figs. 9–11) are obtained at 1 Hz following 10 beats (i.e., at steady state).

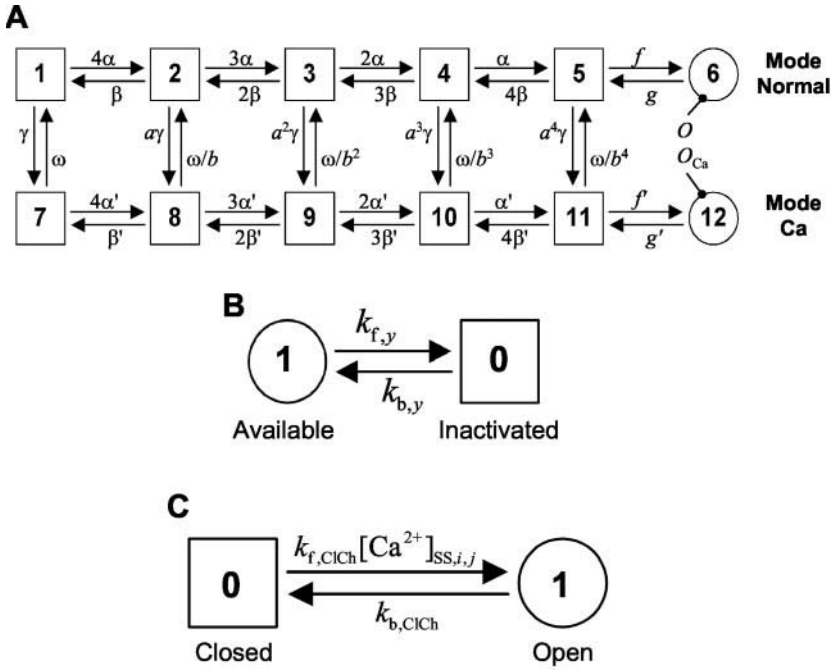

FIGURE 12 State diagrams for the LCC and the ClCh channel Markov models. (*A*) State model of the mode switching and voltage activation processes of the LCC channel model. The states in the upper row encompass Mode Normal and the states in the lower row encompass Mode Ca. Open states are labeled *O* and O_{Ca} (states 6 and 12). Depolarization promotes transitions from left to right toward the open states. Elevation of Ca^{2+} in the adjacent subspace promotes transitions into Mode Ca, where transitions into O_{Ca} are rare (for more details see Jafri et al., 1998, and Rice et al., 1999). (*B*) State model for voltage-dependent inactivation of an LCC. Depolarization promotes transitions from the available state (y) to the unavailable state ($1-y$). See Eqs. 6–16 and Table 3 for equations and parameters describing LCC state transitions. (*C*) State model for the ClCh (I_{to2}). Elevation of Ca^{2+} in the adjacent subspace promotes transitions from the closed state into the open state. See Eqs. 17–18 and Table 3 for equations and parameters describing ClCh state transitions.

surface area, is equal to the summation of unitary Cl^- currents over all ClChs

$$I_{to2} = \frac{1}{C_{SA}} \frac{N_{CaRU}}{N_s} \sum_{i=1}^{N_s} \sum_{j=1}^{4} I_{ClCh,i,j} \tag{18}$$

Each RyR channel is represented by the Markov state model developed by Keizer and Smith (1998) and later modified by Rice et al. (1999). Fig. 13 *A* shows the baseline RyR model structure. States 3 and 4 correspond to open states in the baseline model. Under conditions of elevated subspace Ca^{2+}, rapid equilibrium approximations are applied to pairs of states when the transition rates between the pair are ~200-fold faster than the rates exiting the pair (Keizer and Smith, 1998). Fig. 13, *B* and *C* show the five- and four-state equivalent models used and the $[Ca^{2+}]_{SS}$ ranges in which these reduced order models are considered to be valid. The RyR model representations are dynamically switched among the six, five, and four-state representations during the simulation as local Ca^{2+} levels vary. To further reduce computation time, RyR Ca^{2+}-dependent transition rates are bounded below a maximal value corresponding to the rates that occur at a subspace Ca^{2+} level of 50 μM to prevent extremely fast and unrealistic transition rates at high local Ca^{2+} levels (Rice et al., 1999). This bound was not applied to rate k_{12} because it is significantly slower than the other Ca^{2+}-dependent rates, and the constraint of microscopic reversibility does not apply to k_{12} because it is not within a closed loop of states.

The RyR Ca^{2+} release flux in the jth subspace of the ith CaRU is computed as

$$J_{rel,i,j} = \sum_{k=1}^{5} \text{is open}(RyR_{i,j,k}) r_{RyR}([Ca^{2+}]_{JSR,i} - [Ca^{2+}]_{SS,i,j}) \tag{19}$$

where is open($RyR_{i,j,k}$) takes on the value of 1 when the kth RyR in the jth subspace of the ith CaRU is open($RyR_{i,j,k}$ is in state 3, 4, or 3–4) and takes on the value of 0 otherwise; r_{RyR} is the transfer rate of Ca^{2+} through an open RyR; $[Ca^{2+}]_{SS,i,j}$ is the subspace Ca^{2+} concentration in the jth subspace of the ith CaRU; and $[Ca^{2+}]_{JSR,i}$ is the JSR Ca^{2+} concentration in the ith CaRU. J_{rel}, the whole-cell SR release flux, can be calculated by applying Eq. 16 to $J_{rel,i,j}$. This is necessary only when calculating features such as EC coupling gain.

Local Ca^{2+} balance

The Ca^{2+} balance equation for the JSR in the ith CaRU is

$$\frac{d[Ca^{2+}]_{JSR,i}}{dt} = \beta_{JSR,i} \left(J_{tr,i} - \frac{V_{SS}}{V_{JSR}} \sum_{j=1}^{4} J_{rel,i,j} \right) \tag{20}$$

where

$$\beta_{JSR,i} = \left(1 + \frac{[CSQN]_T K_{CSQN}}{(K_{CSQN} + [Ca^{2+}]_{JSR,i})^2} \right)^{-1} \tag{21}$$

is an implementation of the rapid buffering approximation as previously described by Rice et al. (1999). Calsequestrin concentration and Ca^{2+} binding affinity ($[CSQN]_T$ and K_{CSQN}) are based on recent measurements (Shannon et al., 2000). Similarly, Ca^{2+} balance in the 1st, 2nd, 3rd, and 4th subspaces of the ith CaRU are respectively described by

$$\frac{d[Ca^{2+}]_{SS,i,1}}{dt} = \beta_{SS,i,1}(J_{LCC,i,1} + J_{rel,i,1} - J_{xfer,i,1} + J_{iss,i,2,1} + J_{iss,i,4,1}) \tag{22}$$

$$\frac{d[Ca^{2+}]_{SS,i,2}}{dt} = \beta_{SS,i,2}(J_{LCC,i,2} + J_{rel,i,2} - J_{xfer,i,2} + J_{iss,i,3,2} + J_{iss,i,1,2}) \tag{23}$$

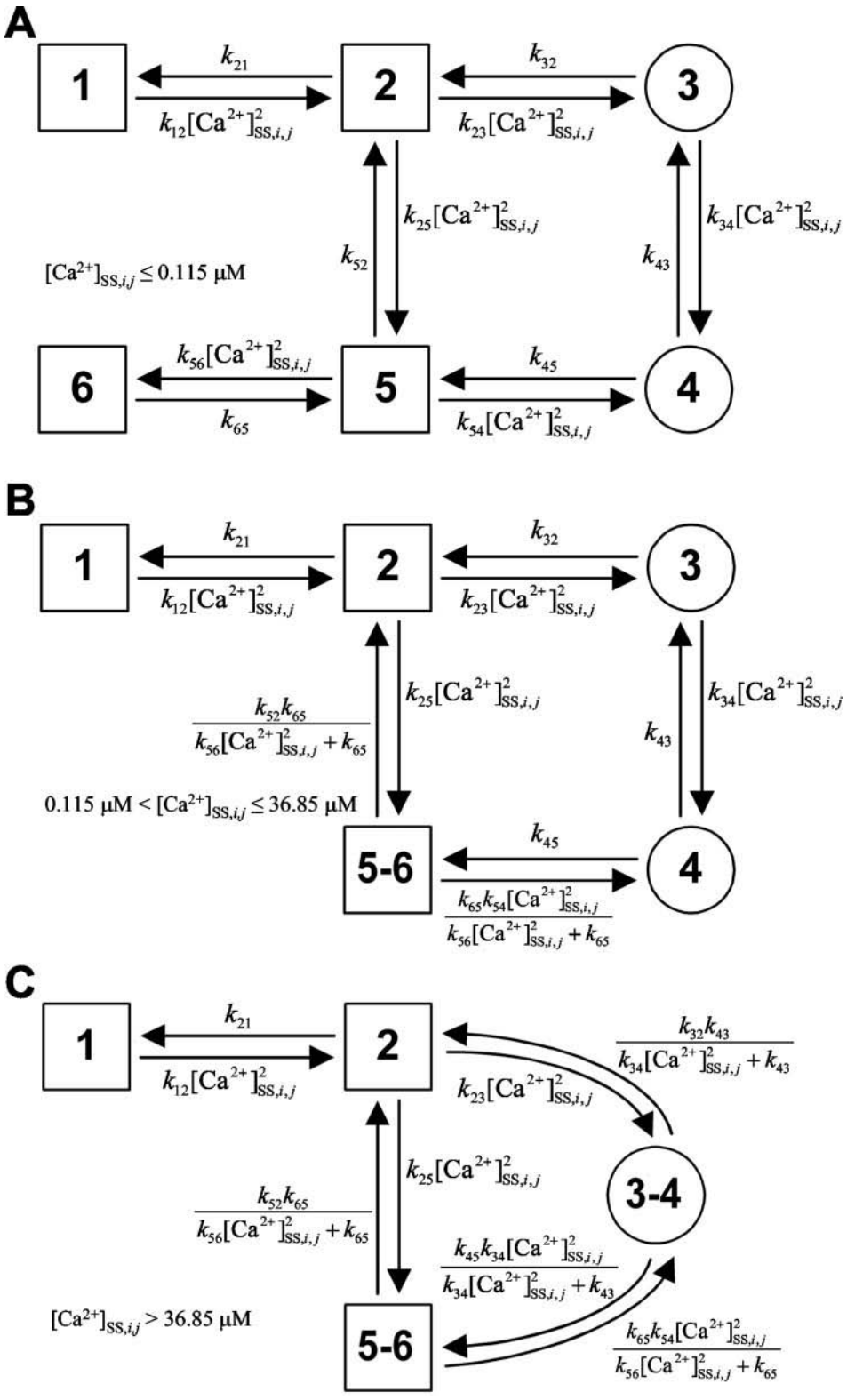

FIGURE 13 State diagrams for the RyR Markov models. (*A*) Baseline RyR model where states 1 and 2 are the resting states, states 3 and 4 are the open states, and states 5 and 6 are the refractory states. It is assumed that each Ca^{2+}-dependent transition is associated with the binding of two Ca^{2+} ions, therefore requiring that four Ca^{2+} ions bind to reach the open state. This model is implemented when subspace Ca^{2+} concentration is $<0.115\ \mu M$. See Table 4 for values of the rate constants. (*B*) Approximation of the model in panel *A* where it has been assumed that states 5 and 6 are in rapid equilibrium, and are therefore merged into a single state. This model is implemented when subspace Ca^{2+} concentration is in the range of 0.115–36.85 μM. (*C*) Approximation of the model in panel *B* where it has been assumed that states 3 and 4 are in rapid equilibrium. This model is implemented when subspace Ca^{2+} concentration is $>36.85\ \mu M$.

$$\frac{d[Ca^{2+}]_{SS,i,3}}{dt} = \beta_{SS,i,3}(J_{LCC,i,3} + J_{rel,i,3} - J_{xfer,i,3} + J_{iss,i,4,3} + J_{iss,i,2,3}) \quad (24)$$

$$\frac{d[Ca^{2+}]_{SS,i,4}}{dt} = \beta_{SS,i,4}(J_{LCC,i,4} + J_{rel,i,4} - J_{xfer,i,4} + J_{iss,i,1,4} + J_{iss,i,3,4}) \quad (25)$$

where

$$J_{LCC,i,j} = \frac{-I_{LCC,j,i}}{2FV_{SS}} \quad (26)$$

and

$$\beta_{SS,i,j} = \left(1 + \frac{[BSR]_T K_{BSR}}{(K_{BSR} + [Ca^{2+}]_{SS,i,j})^2} + \frac{[BSL]_T K_{BSL}}{(K_{BSL} + [Ca^{2+}]_{SS,i,j})^2}\right)^{-1} \quad (27)$$

describes rapid equilibrium between Ca^{2+} and membrane-bound Ca^{2+} buffers (Rice et al., 1999).

Global ionic fluxes

All of the global currents and ionic fluxes that are incorporated into the local control myocyte model have been described fully in previous work. Table 6 provides references for previously published mathematical model descriptions and parameters, and any parameters that differ in the present implementation from the referenced version of the model are provided.

Global ionic flux balance and membrane potential

Intracellular concentrations of Na^+, K^+, NSR Ca^{2+}, and cytosolic Ca^{2+} are described respectively by

$$\frac{d[Na^+]_i}{dt} = \frac{-C_{SA}}{V_{cyto}F}(I_{Na} + I_{Na,b} + 3I_{NaCa} + 3I_{NaK}) \quad (28)$$

$$\frac{d[K^+]_i}{dt} = \frac{-C_{SA}}{V_{cyto}F}(I_{Kr} + I_{Ks} + I_{to1} + I_{Kl} + I_{Kp} - 2I_{NaK}) \quad (29)$$

$$\frac{d[Ca^{2+}]_{NSR}}{dt} = \frac{V_{cyto}}{V_{NSR}}J_{up} - \frac{V_{JSR}}{V_{NSR}}J_{tr} \quad (30)$$

$$\frac{d[Ca^{2+}]_{cyto}}{dt} = \beta_{cyto}\left\{\frac{-C_{SA}}{2V_{cyto}F}(I_{Ca,b} + I_{p(Ca)} - 2I_{NaCa}) + \frac{V_{SS}}{V_{cyto}}J_{xfer} - J_{up} - J_{trpn}\right\} \quad (31)$$

where

$$\beta_{cyto} = \left(1 + \frac{[CMDN]_T K_{CMDN}}{(K_{CMDN} + [Ca^{2+}]_{cyto})^2}\right)^{-1} \quad (32)$$

describes Ca^{2+} buffering by calmodulin (Winslow et al., 1999).

The membrane potential is calculated as

$$\frac{dV_m}{dt} = -(I_{Na} + I_{CaL} + I_{Kr} + I_{Ks} + I_{to1} + I_{Kl} + I_{Kp} + I_{to2} + I_{NaK} + I_{NaCa} + I_{p(Ca)} + I_{Ca,b} + I_{Na,b}) \quad (33)$$

where all currents are expressed in units of pA pF^{-1}.

APPENDIX II

Local control myocyte simulation algorithm

Each model state variable (SV) is a member of one of the following three groups: 1) global, 2) CaRU-compartment, or 3) CaRU-random. The JSR-NSR, subspace-cytosol, and subspace-sarcolemmal borders define the boundaries of a CaRU. Global SVs represent quantities external to the CaRU boundaries, including membrane potential (V_m), cytosolic ion concentrations (Ca^{2+}, K^+, and Na^+), and NSR Ca^{2+} concentration. In addition, Hodgkin-Huxley-type gating variables (e.g., m, h, and j for I_{Na}) and Markov model states (e.g., C_1, C_2, C_3, I, and O for I_{Kr}) associated with currents that exist entirely outside of the CaRUs are global. The CaRU-compartment SVs are Ca^{2+} concentrations in the JSR and in each SS of every CaRU, and are thus local states. CaRU-random SVs take on the value of the occupied states in single channel Monte Carlo simulations (LCC, RyR, and ClCh), and are therefore also local states. Each group of SVs requires its own simulation sub-algorithm. First, each of these sub-algorithms is described, and then we show how they interact to form the complete simulation of the local control model.

Let global SVs be denoted by the vector $\mathbf{x}(t)$. Let CaRU-compartment SVs and CaRU-random SVs within the ith CaRU be denoted by the vectors $\mathbf{y}_i(t)$ and $\mathbf{z}_i(t)$, respectively. N_{CaRU} is the number of CaRUs in the myocyte and N_s is the number of CaRUs actually simulated. The difference in N_{CaRU} and N_s arises from a useful approximation described below.

The coupled system of differential equations for the global SVs is represented by

$$\dot{\mathbf{x}} = f^{\mathbf{x}}(t, \mathbf{x}, \mathbf{y}_1, \ldots, \mathbf{y}_{N_s}, \mathbf{z}_1, \ldots, \mathbf{z}_{N_s}) \quad (34)$$

where $f^{\mathbf{x}}$ denotes the function defining the velocity field (time derivative) of $\mathbf{x}$. Note that the right-hand side of Eq. 34 depends upon SVs from all three groups. Integration of global SVs is performed with the Runge-Kutta-Merson fourth-order adaptive step method (RK4M) (Kubicek and Marek, 1983). The RK4M advances the global state vector in time from $\mathbf{x}(t)$ to $\mathbf{x}(t + h_{\mathbf{x}})$, where $h_{\mathbf{x}}$ denotes a global time step, by subdividing $h_{\mathbf{x}}$ into Euler-type intermediate steps (sub-steps). Fig. 14 shows the relationship among different time steps used throughout the simulation algorithm. Equations 35 through 39 compose a single RK4M time step for this system and make use of the compact notation $f^{\mathbf{x}}([t\mathbf{xyz}]^n) = f^{\mathbf{x}}(t^n, \mathbf{x}^n, \mathbf{y}_1^n, \ldots, \mathbf{y}_{N_s}^n, \mathbf{z}_1^n, \ldots, \mathbf{z}_{N_s}^n)$:

$$\mathbf{v}^{n+1/3} = \mathbf{x}^n + \frac{h_{\mathbf{x}}^n}{3}f^{\mathbf{x}}([t\mathbf{xyz}]^n) \quad (35)$$

$$\hat{\mathbf{v}}^{n+1/3} = \mathbf{x}^n + \frac{h_{\mathbf{x}}^n}{3}\left(\frac{f^{\mathbf{x}}([t\mathbf{xyz}]^n) + f^{\mathbf{x}}([t\mathbf{vyz}]^{n+1/3})}{2}\right) \quad (36)$$

$$\mathbf{v}^{n+1/2} = \mathbf{x}^n + \frac{h_{\mathbf{x}}^n}{2}\left(\frac{f^{\mathbf{x}}([t\mathbf{xyz}]^n) + 3f^{\mathbf{x}}([t\hat{\mathbf{v}}\mathbf{yz}]^{n+1/3})}{4}\right) \quad (37)$$

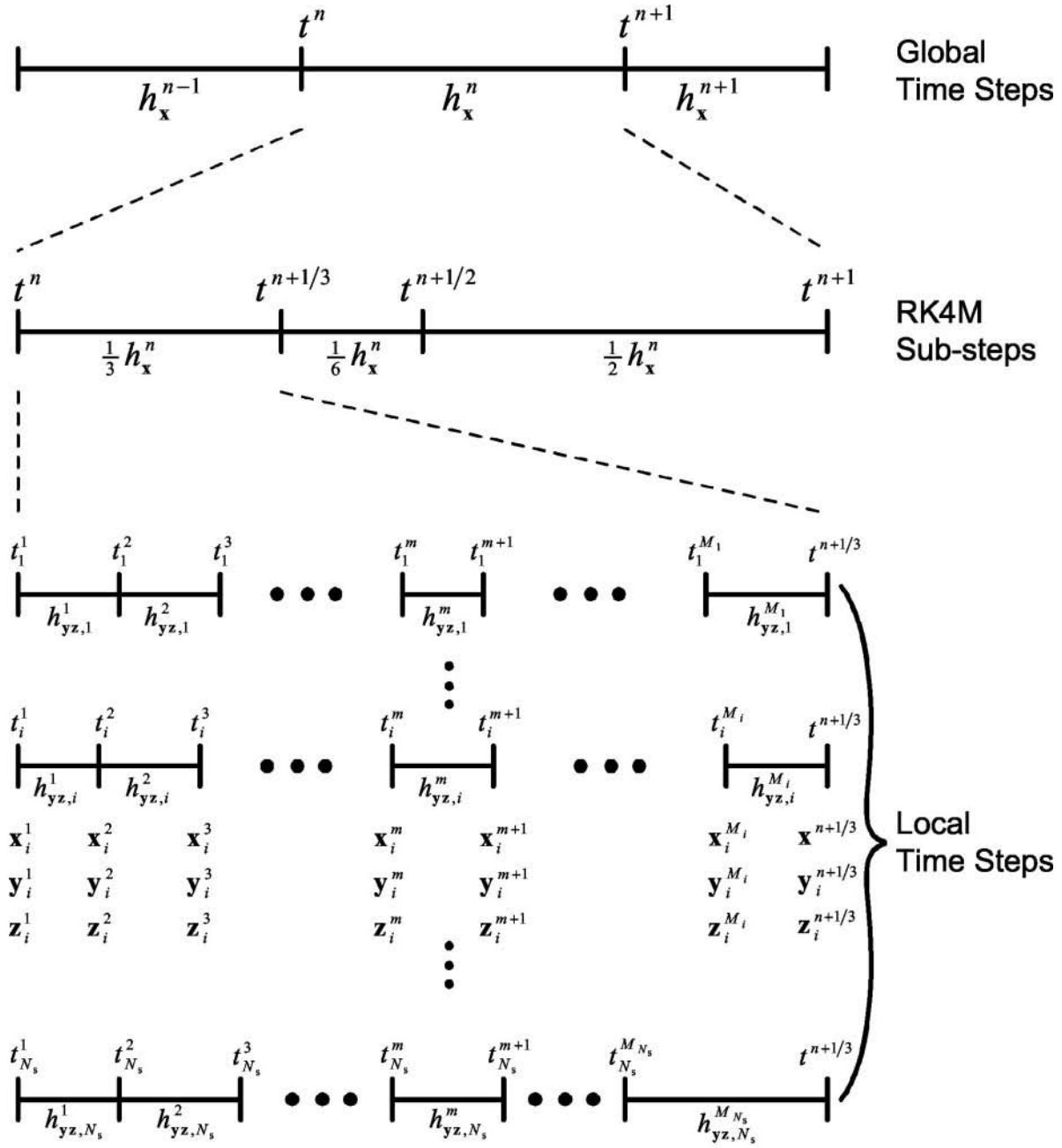

FIGURE 14 Time-stepping scheme for the local control myocyte simulation algorithm. The global state vector is advanced in time from t^{n} to t^{n+1} over the global time step $h_{\mathbf{x}}^{n}$, where n is an index to global time steps (i.e., $h_{\mathbf{x}}^{n}$ is the nth global time step). Each global time step is divided into RK4M substeps, which are themselves divided into local time steps. CaRU-compartment and CaRU-random state vectors are simulated along local time steps, which are determined independently within each CaRU. The local time step in the ith CaRU between times t_i^m and t_i^{m+1} is denoted $h_{\mathbf{yz},i}^{m}$, where m is an index to local time steps. The index M_i refers to the last local time step in the ith CaRU within the bounds of the encompassing global time step, and N_s is the number of CaRUs included in the Monte Carlo simulation.

$$\hat{\mathbf{v}}^{n+1} = \mathbf{x}^{n} + h_{\mathbf{x}}^{n}\left(\frac{f^{\mathbf{x}}([t\mathbf{xyz}]^{n}) - 3f^{\mathbf{x}}([t\hat{\mathbf{v}}\mathbf{yz}])^{n+1/3}) + 4f^{\mathbf{x}}([t\mathbf{vyz}]^{n+1/2})}{2}\right) \tag{38}$$

$$\hat{\mathbf{v}}^{n+1} = \mathbf{x}^{n} + h_{\mathbf{x}}^{n}\left(\frac{f^{\mathbf{x}}([t\mathbf{xyz}]^{n}) + 4f^{\mathbf{x}}([t\mathbf{vyz}]^{n+1/2}) + f^{\mathbf{x}}([t\mathbf{vyz}])^{n+1}}{6}\right) \tag{39}$$

where $t^{n+1/p} = t^n + h_x^n/p$, $p = 3, 2, 1$ denote intermediate times within the nth global time step h_x^n. Similarly, we have made use of the notation $\mathbf{u}^{n+1/p} = \mathbf{u}(t^n + h_x^n/p)$, where $\mathbf{u}$ denotes any state vector. Equation 39 yields the fourth-order estimate of the solution, $x^{n+1} = \hat{\mathbf{v}}^{n+1}$. The solution is accepted if the embedded truncation error estimate

$$E = \|\mathbf{v}^{n+1} - \hat{\mathbf{v}}^{n+1}\|/5 \tag{40}$$

is less than the tolerance (ε) for each global SV, otherwise Eqs. 35–39 are reevaluated with a smaller h_x^n determined by

$$h_{x,new}^n = 0.85 h_{x,old}^n (\varepsilon/|E|)^{0.2} \tag{41}$$

Equation 41 is also used to increase the global time step if the solution over the previous step has been accepted. The errors for each SV are normalized to ensure that each is equally weighted in the truncation error calculation. Global step size is normally limited by the time-rate-of-change of the global SVs, but is not limited by fast dynamics within CaRUs. An important feature of this procedure is that every equation evaluation (of Eqs. 35–39) yields an estimated solution at the intermediate time step (i.e., each $\mathbf{v}$ is an estimate of $\mathbf{x}$, e.g., $\mathbf{x}^{n+1/2} \approx \mathbf{v}^{n+1/2}$). We make use of this property when calculating fluxes that cross CaRU boundaries (see below). The left-hand sides of Eqs. 36 and 39 are denoted with a caret symbol (i.e., $\hat{\mathbf{v}}$) to indicate that these are refinements of the estimates obtained in the immediately preceding equation (at the same time point).

The simulation of a CaRU does not require knowledge of events occurring in any other CaRU within the span of a single global time step (i.e., CaRUs are independent on the interval $[t, t + h_x]$), which allows for parallelization of this part of the algorithm. The solution of both CaRU-compartment and CaRU-random SVs within the ith CaRU is advanced in increments of the local time step, $h_{yz,i}$. The coupled system of differential equations for the CaRU-compartment SVs of the ith CaRU is represented by

$$\dot{\mathbf{y}}_i = f^y(t, \mathbf{x}, \mathbf{y}_i, \mathbf{z}_i) \tag{42}$$

where f^y denotes the function defining the velocity field of $\mathbf{y}_i$ (for any i). Integration of CaRU-compartment SVs is performed with the second-order trapezoidal method. The trapezoidal method is chosen because it provides higher-order accuracy than the Euler method without the need to further subdivide the local time step. The solution is advanced in time as follows:

$$\mathbf{w}_i^{m+1} = \mathbf{y}_i^m + h_{yz,i}^m f^y(t_i^m, \mathbf{x}_i^m, \mathbf{y}_i^m, \mathbf{z}_i^m) \tag{43}$$

$$\mathbf{y}_i^{m+1} = \mathbf{y}_i^m + h_{yz,i}^m \left(\frac{f^y(t_i^m, \mathbf{x}_i^m, \mathbf{y}_i^m, \mathbf{z}_i^m) + f^y(t_i^{m+1}, \mathbf{x}_i^{m+1}, \mathbf{w}_i^{m+1}, \mathbf{z}_i^m)}{2} \right) \tag{44}$$

where $\mathbf{y}_i^m = \mathbf{y}_i(t_i^m)$, $\mathbf{y}_i^{m+1} = \mathbf{y}_i(t_i^m + h_{yz,i}^m)$, and $h_{yz,i}^m$ is the mth local time step within the ith CaRU. Note that while t and $\mathbf{x}$ are global, the notation t_i^m and $\mathbf{x}_i^m$ are used locally because local time steps are not synchronized across CaRUs, i.e., $h_{yz,i}^m \neq h_{yz,j}^m$, which implies $t_i^m \neq t_j^m$ and $\mathbf{x}_i^m \neq \mathbf{x}_j^m$. The counter variable m restarts at the beginning of each RK4M substep (see Fig. 14). The CaRU-random SV vector, $\mathbf{z}_i^m$, is not updated to $\mathbf{z}_i^{m+1}$ within Eq. 44, rather $\mathbf{z}_i^m$ is assumed to remain constant during the local time step, and is updated immediately after the CaRU-compartment SVs have been updated to $\mathbf{y}_i^{m+1}$ (see below for more details). Within Eqs. 43 and 44, $\mathbf{x}_i^m$ is calculated by linearly interpolating from values previously calculated at the beginning and ending time of the current RK4M substep (Fig. 14). For example, if $t^{n+1/3} < t_i^m < t^{n+1/2}$, then $\mathbf{x}_i^m$ is interpolated using the current estimates of the interval endpoints $\mathbf{x}^{n+1/3} \approx \hat{\mathbf{v}}^{n+1/3}$ and $\mathbf{x}^{n+1/2} \sim \mathbf{v}^{n+1/2}$.

A Monte Carlo simulation is run to update $\mathbf{z}_i^m$ to $\mathbf{z}_i^{m+1}$ over the local time step $h_{yz,i}^m$ in the ith CaRU. It is assumed that CaRU-compartment SVs remain constant over the duration of a single local time step. Let $j = 1, 2, 3, \ldots$ index the group of CaRU-random variables for the ith CaRU (i.e., each j is an index to a particular channel or Markov process). Let $r_{i,j}^k$, $k = 1, 2, 3, \ldots$ denote the transition rate for the jth channel in the ith CaRU from its currently occupied state into state k. Also, let $\nu_{i,j} = \Sigma_k r_{i,j}^k$. Then the probability that the jth channel made a state transition within the time step $h_{yz,i}^m$ is

$$p_{i,j} \approx \nu_{i,j} h_{yz,i}^m \tag{45}$$

and the probability that no transition occurred is therefore $1 - \nu_{i,j} h_{yz,i}^m$. Then, by conditioning on whether a change of state has occurred, the probability that the jth channel entered state k within the time step $h_{yz,i}^m$ is

$$p_{i,j}^k \approx (\nu_{i,j} h_{yz,i}^m)(r_{i,j}^k/\nu_{i,j}) = h_{yz,i}^m r_{i,j}^k \tag{46}$$

For each j, a standard uniform random variable is generated and is used to determine into which state the process transits, if a transition occurs, based on Eqs. 45 and 46. This process is completed for each i (each CaRU), and the newly occupied states are recorded as $\mathbf{z}_i^{m+1}$.

The local time step $h_{yz,i}^m$ is determined based on two criteria: 1) to ensure that the approximate relation of Eq. 45 is valid, and 2) to ensure that dynamics of Ca^{2+} within the CaRUs (CaRU-compartments SVs) are adequately captured. The first criterion is satisfied by imposing the condition

$$h_{yz,i}^m \leq \frac{tol}{\max_j(\nu_{i,j})} \tag{47}$$

With $tol = 0.05$, $h_{yz,i}^m$ is no greater than 5% of the expected waiting time until the next transition of the channel with the fastest exit rate. Because $p_{i,j} = 1 - \exp(-\nu_{i,j} h_{yz,i}^m) \approx \nu_{i,j} h_{yz,i}^m$, the maximum transition probability is $p_{i,j} = 1 - \exp(-tol) = 0.04877 \approx tol = 0.05$. A bound on the error in $p_{i,j}$ due to the approximation of Eq. 45 is therefore 0.00133. The second criterion is satisfied by imposing the constraint: if Ca^{2+} concentration in any subspace compartment of the ith CaRU is >1.5 μM, then $h_{yz,i}^m \leq 5$ μs, else $h_{yz,i}^m \leq 10$ μs. In addition to these criteria, local time steps are occasionally shortened to synchronize with the encompassing global time step, h_x^n.

Using the algorithmic components described above, the local control myocyte simulation advances the solution from the states defined by $\mathbf{x}(t)$, $\mathbf{y}_1(t), \ldots, \mathbf{y}_{N_s}(t)$, $\mathbf{z}_1(t), \ldots, \mathbf{z}_{N_s}(t)$ to $\mathbf{x}(t + h_x^n)$, $\mathbf{y}_1(t + h_x^n), \ldots, \mathbf{y}_{N_s}(t + h_x^n)$, $\mathbf{z}_1(t + h_x^n), \ldots, \mathbf{z}_{N_s}(t + h_x^n)$, respectively, in the following manner:

1. Choose h_x^n (initial guess or based on E of previous RK4M step, Eq. 40).
2. Calculate $\mathbf{v}^{n+1/3}$ (Eq. 35).
3. Loop over each i:
   a) While $t_i^m < t^{n+1/3}$ do:
      i. Choose $h_{yz,i}^m$ (Eq. 47 and other bounds).
      ii. Calculate $\mathbf{x}_i^m$ and $\mathbf{x}_i^{m+1}$ (interpolate between $\mathbf{x}^n$ and $\mathbf{v}^{n+1/3}$).
      iii. Calculate $\mathbf{y}_i^{m+1}$ (Eqs. 43–44).
      iv. Calculate $\mathbf{z}_i^{m+1}$ (Eqs. 45–46 and uniform random variables).
      v. Set $m = m + 1$.
      End While;
   b) Set $\mathbf{y}^{n+1/3} = \mathbf{y}_i^{m+1}$; Set $\mathbf{z}^{n+1/3} = \mathbf{z}_i^{m+1}$.
   End Loop over i;
4. Calculate $\hat{\mathbf{v}}^{n+1/3}$ (Eq. 36) and $\mathbf{v}^{n+1/2}$ (Eq. 37).
5. Repeat procedure as described in step 3 on the interval $[t^{n+1/3}, t^{n+1/2}]$.
6. Calculate $\mathbf{v}^{n+1}$ (Eq. 38).
7. Repeat procedure as described in step 3 on the interval $[t^{n+1/2}, t^{n+1}]$.
8. Calculate $\hat{\mathbf{v}}^{n+1}$ (Eq. 39).
9. If E (Eq. 40) is acceptable, then
   a) $\mathbf{x}^{n+1} = \hat{\mathbf{v}}^{n+1}$ (update global SVs).
   b) Set $n = n + 1$.
   c) Set new global time step h_x^{n+1} (Eq. 41).
   d) Goto step 1 (to continue)
   Else
   a) revise h_x^n, (Eq. 41).
   b) Goto step 1 (to repeat).

The loops performed over all CaRUs (*i*'s) can be parallelized (steps 3, 5, and 7). Sensible reductions in the number of necessary calculation can be made during many of these steps. For example, in step 3.a.ii of the CaRU simulation, the only global SVs that need be interpolated are NSR and cytosolic Ca^{2+} concentrations, and V_m.

Equations 45 and 46 give probabilities that a transition has occurred sometime during the local time step, $h^m_{\mathbf{yz},i}$. It is always assumed that the state transition occurs exactly at time $t^m_i + h^m_{\mathbf{yz},i}$ (i.e., $\mathbf{z}^m_i$ is updated to $\mathbf{z}^{m+1}_i$ after Eq. 44 is evaluated). Discretizing the Markov process in this manner introduces an additional source of approximation error. The expected waiting time, denoted $E[T_{i,j}]$, until the *j*th channel in the *i*th CaRU exits its current state is $1/\nu_{i,j}$. When the process is discretized, the waiting time follows a geometric distribution, such that

$$E[T_{i,j}] = \sum_{k=1}^{\infty} k h^m_{\mathbf{yz},i}(1 - p_{i,j})^{k-1} p_{i,j} = \frac{h^m_{\mathbf{yz},i}}{p_{i,j}} \qquad (48)$$

In general, Eq. 48 would not yield an expected waiting time of exactly $1/\nu_{i,j}$. However, if the approximate expression for $p_{i,j}$ defined by Eq. 45 and used in this algorithm is substituted into Eq. 48, the desired result is obtained, i.e., $E[T_{i,j}] = 1/\nu_{i,j}$.

When the subspace Ca^{2+} level is high, the local time step for a CaRU is limited mainly by the fast transition rates of the RyRs. Computational time is reduced by about an order of magnitude by making use of the rapid equilibrium approximation for pairs of states when the transition rates between the pair are relatively fast compared to the rates exiting the pair (Keizer and Smith, 1998). The six-state RyR models are converted to lower-order (five- or four-state) models dynamically under conditions of high local Ca^{2+} when the approximation is valid. In addition, some transition rates are bounded with a maximum value (in a manner that maintains microscopic reversibility) to prevent extremely fast and unrealistic transition rates at high local Ca^{2+} levels (Rice et al., 1999). For details, see the RyR model description in Appendix I.

An additional reduction in computation time can be achieved by simulating only a subset of CaRUs. Every evaluation of $f^{\mathbf{x}}$ (Eq. 34) requires that I_{CaL}, J_{tr}, J_{xfer}, and I_{to2} are calculated by summing over all of the respective unitary currents/fluxes in each CaRU (see Eqs. 2, 5, 16, and 18). Simulation of only a subset of the full population of CaRUs dramatically reduces simulation time. A reduction of N_s will increase the stochastic gating noise in macroscopic I_{CaL}, and hence in V_m and most global SVs. However, the level of noise in these signals remains acceptably low for values of $N_s \ll N_{CaRU}$, making this a very useful and time-saving approximation. During the application of 1-Hz current stimuli, one second of model simulation time requires ~40 min of run time when implemented in parallel on 10 SGI Power Challenge R10,000 processors with only 10% of the total population of CaRUs included in the Monte Carlo simulation (i.e., $N_{CaRU} = 12{,}500$ and $N_s = 1250$). Most simulations presented in this study were performed with 20% of the CaRUs included in the Monte Carlo simulation. At this approximation level, repeated runs showed minimal variation (e.g., error bars in Figs. 3 *B* and 7 *A*). L-type Ca^{2+} currents shown in Fig. 3 *A* were simulated without using this approximation (i.e., 100% of the CaRUs were simulated), and therefore, the noise in these signals is representative of channel gating noise for the entire population of LCCs.

Uniform random variables are obtained using the Numerical Recipes function `ran2` (Press et al., 1992). This generator has a period $>2 \times 10^{18}$ with added safeguards designed to eliminate possible serial correlations in the sequence of uniform deviates. An independent sequence is generated for each simulated channel and each sequence is initialized by generating seeds with the Numerical Recipes function `ran1` (Press et al., 1992). At the beginning of each global time step, all random sequence seeds are stored. If a global time step is rejected in step 9 of the simulation algorithm, the random sequence seeds are reset to the stored values before repeating that step (with a smaller step size) to ensure that the trajectory of the Monte Carlo simulation is not artificially influenced or altered by the decision to accept or reject global time steps based on truncation error (Eq. 40).

The validity of the simulation algorithm was tested by applying a combined voltage- and Ca^{2+} -clamp protocol. From a −100 mV holding potential, voltage is stepped to 0 mV for 50 ms, and then returned to the holding potential. Concurrently, Ca^{2+} in all subspace compartments is clamped at 0.1 mM, stepped to 20 mM for 50 ms, and then returned to 0.1 mM. RyR and LCC open probability determined using the local control model algorithm are nearly the same as those obtained by solving the associated set of ordinary differential equations for this protocol, with slight deviations due only to the presence of gating noise in the local control simulation (data not shown). An additional test is performed to ensure Ca^{2+} flux between individual CaRUs and the whole cell are correctly handled. Total cell Ca^{2+} (in all compartments, including both free and bound Ca^{2+}) is calculated at each point in time by: 1) summing over all cellular compartments, and 2) tracking incremental changes in total Ca^{2+} based on set sarcolemmal Ca^{2+} flux. These values differ by $<0.05\%$ after a 10-s simulation of APs paced at 1 Hz (data not shown).

This work was supported by National Institutes of Health Grants RO1 HL60133 and P50 HL52307, and by the Whitaker Foundation.

REFERENCES

Ahmmed, G. U., P. H. Dong, G. Song, N. A. Ball, Y. Xu, R. A. Walsh, and N. Chiamvimonvat. 2000. Changes in Ca^{2+} cycling proteins underlie cardiac action potential prolongation in a pressure-overloaded guinea pig model with cardiac hypertrophy and failure. *Circ. Res.* 86:558–570.

Arkin, A., J. Ross, and H. H. McAdams. 1998. Stochastic kinetic analysis of developmental pathway bifurcation in phage λ-infected *Escherichia coli* cells. Genetics. 149:1633–1648.

Bassani, J. W., W. Yuan, and D. M. Bers. 1995. Fractional SR Ca release is regulated by trigger Ca and SR Ca content in cardiac myocytes. *Am. J. Physiol. Cell Physiol.* 268:C1313–C1319.

Bers, D. M. 1993. Excitation Contraction Coupling and Cardiac Contractile Force. Kluwer Academic Press, Boston.

Bers, D. M., and E. Perez-Reyes. 1999. Ca channels in cardiac myocytes: structure and function in Ca influx and intracellular Ca release. *Cardiovasc Res.* 42:339–360.

Beuckelmann, D. J., and W. G. Wier. 1988. Mechanism of release of calcium from sarcoplasmic reticulum of guinea-pig cardiac cells. *J. Physiol. (Lond).* 405:233–255.

Cannell, M., J. Berlin, and W. Lederer. 1987. Effect of membrane potential changes on the calcium transient in single rat cardiac muscle cells. *Science.* 283:1419–1423.

Cannell, M., H. Cheng, and W. Lederer. 1984. Spatial non-uniformities in $[Ca^{2+}]_i$ during excitation-contraction coupling in cardiac myocytes. *Biophys J.* 67:1942–1956.

Cannell, M. B., H. Cheng, and W. J. Lederer. 1995. The control of calcium release in heart muscle. *Science.* 268:1045–1049.

Cannell, M. B., and C. Soeller. 1997. Numerical analysis of ryanodine receptor activation by L-type channel activity in the cardiac muscle diad. *Biophys J.* 73:112–122.

Cheng, H., M. Fill, H. Valdivia, and W. J. Lederer. 1995. Models of Ca^{2+} release channel adaptation. *Science.* 267:2009–2010.

Cheng, H., W. J. Lederer, and M. B. Cannell. 1993. Calcium sparks: elementary events underlying excitation-contraction coupling in heart muscle. *Science.* 262:740–744.

Cleemann, L., and M. Morad. 1991. Role of the Ca^{2+} channel in cardiac excitation-contraction coupling in the rat: evidence from Ca^{2+} transients and contraction. *J. Physiol.* 432:283–312.

Collier, M., P. Levesque, J. Kenyon, and J. Hume. 1996. Unitary Cl^- channels activated by cytoplasmic Ca^{2+} in canine ventricular myocytes. *Circ. Res.* 78:936–944.

Collier, M. L., A. P. Thomas, and J. R. Berlin. 1999. Relationship between L-type Ca^{2+} current and unitary sarcoplasmic reticulum Ca^{2+} release events in rat ventricular myocytes. *J. Physiol. (Lond.).* 516:117–128.

Davare, M. A., V. Avdonin, D. D. Hall, E. M. Peden, A. Burette, R. J. Weinberg, M. C. Horne, T. Hoshi, and J. W. Hell. 2001. A beta 2 adrenergic receptor signaling complex assembled with the Ca^{2+} channel Cav1.2. *Science.* 293:98–101.

DelBridge, L. M., J. W. Bassani, and D. M. Bers. 1996. Steady-state twitch Ca^{2+} fluxes and cytosolic Ca^{2+} buffering in rabbit ventricular myocytes. *Am. J. Physiol. Cell Physiol.* 270:C192–C199.

Faber, G. M., and Y. Rudy. 2000. Action potential and contractility changes in $[Na+]_i$ overloaded cardiac myocytes: a simulation study. *Biophys. J.* 78:2392–2404.

Fabiato, A. 1985. Time and calcium dependence of activation and inactivation of calcium-induced release of calcium from the sarcoplasmic reticulum of a skinned canine cardiac Purkinje cell. *J. Gen. Physiol.* 85:247–289.

Fox, J. J., J. L. McHarg, and R. F. Gilmour, Jr. 2002. Ionic mechanism of electrical alternans. *Am. J. Physiol. Heart Circ. Physiol.* 282: H516–H530.

Franzini-Armstrong, C., F. Protasi, and V. Ramesh. 1999. Shape, size, and distribution of Ca^{2+} release units and couplons in skeletal and cardiac muscles. *Biophys. J.* 77:1528–1539.

Gomez, A. M., H. H. Valdivia, H. Cheng, M. R. Lederer, L. F. Santana, M. B. Cannell, S. A. McCune, R. A. Altschuld, and W. J. Lederer. 1997. Defective excitation-contraction coupling in experimental cardiac hypertrophy and heart failure. *Science.* 276:800–806.

Greenstein, J. L., and R. L. Winslow. 2001a. Probing the role of excitation-contraction coupling properties on the ventricular action potential. *Ann. Biomed. Eng.* 29:S-51.

Greenstein, J. L., and R. L. Winslow. 2001b. Integration of a stochastic model of local calcium control with a simulation of the cardiac ventricular action potential. *Biophys. J.* 80:593*a*. (Abstr.).

Greenstein, J. L., R. Wu, S. Po, G. F. Tomaselli, and R. L. Winslow. 2000. Role of the calcium-independent transient outward current I_{to1} in shaping action potential morphology and duration. *Circ Res.* 87:1026–1033.

Gyorke, S., and M. Fill. 1993. Ryanodine receptor adaptation: control mechanism of Ca^{2+}-induced Ca^{2+} release in heart. *Science.* 260: 807–809.

Hadley, R. W., and J. R. Hume. 1987. An intrinsic potential-dependent inactivation mechanism associated with calcium channels in guinea-pig myocytes. *J. Physiol.* 389:205–222.

Handrock, R., F. Schroder, S. Hirt, A. Haverich, C. Mittmann, and S. Herzig. 1998. Single-channel properties of L-type calcium channels from failing human ventricle. *Cardiovasc. Res.* 37:445–455.

He, J.-Q., M. Conklin, J. Foell, M. Wolff, R. Haworth, R. Coronado, and T. Kamp. 2001. Reduction in density of transverse tubules and L-type Ca^{2+} channels in canine tachycardia-induced heart failure. *Cardiovasc. Res.* 49:298–307.

Herzig, S., P. Patil, J. Neumann, C.-M. Staschen, and D. Yue. 1993. Mechanisms of β-adrenergic stimulation of cardiac Ca^{2+} channels revealed by discrete-time Markov analysis of slow gating. *Biophys. J.* 65:1599–1612.

Hobai, I. A., and B. O'Rourke. 2001. Decreased sarcoplasmic reticulum calcium content is responsible for defective excitation-contraction coupling in canine heart failure. *Circulation.* 103:1577–1584.

Jafri, S., J. J. Rice, and R. L. Winslow. 1998. Cardiac Ca^{2+} dynamics: the roles of ryanodine receptor adaptation and sarcoplasmic reticulum load. *Biophys. J.* 74:1149–1168.

Janczewski, A. M., H. A. Spurgeon, M. D. Stern, and E. G. Lakatta. 1995. Effects of sarcoplasmic reticulum Ca^{2+} load on the gain function of Ca^{2+} release by Ca^{2+} current in cardiac cells. *Am. J. Physiol. Heart Circ. Physiol.* 268:H916–H9120.

Kääb, S., H. B. Nuss, N. Chiamvimonvat, B. O'Rourke, P. H. Pak, D. A. Kass, E. Marban, and G. F. Tomaselli. 1996. Ionic mechanism of action potential prolongation in ventricular myocytes from dogs with pacing-induced heart failure. *Circ. Res.* 78:262–273.

Keizer, J., and L. Levine. 1996. Ryanodine receptor adaptation and Ca^{2+}-induced Ca^{2+} release-dependent Ca^{2+} oscillations. *Biophys. J.* 71: 3477–3487.

Keizer, J., and G. D. Smith. 1998. Spark-to-wave transition: saltatory transmission of calcium waves in cardiac myocytes. *Biophys. Chem.* 72:87–100.

Kubicek, M., and M. Marek. 1983. Computational Methods in Bifurcation Theory and Dissipative Structures. Springer-Verlag, New York.

Langer, G. A., and A. Peskoff. 1996. Calcium concentration and movement in the diadic cleft space of the cardiac ventricular cell. *Biophys. J.* 70:1169–1182.

Li, G.-R., B. Yang, J. Feng, R. F. Bosch, M. Carrier, and S. Nattel. 1999. Transmembrane I_{Ca} contributes to rate-dependent changes of action potentials in human ventricular myocytes. *Am. J. Physiol. Heart Circ. Physiol.* 276:H98–H106.

Lindner, M., E. Erdmann, and D. J. Beuckelmann. 1998. Calcium content of the sarcoplasmic reticulum in isolated ventricular myocytes from patients with terminal heart failure. *J. Mol. Cell Cardiol.* 30:743–749.

Linz, K. W., and R. Meyer. 1998. Control of L-type calcium current during the action potential of guinea-pig ventricular myocytes. *J. Physiol. (Lond.).* 513:425–442.

Lopez-Lopez, J. R., P. S. Shacklock, C. W. Balke, and W. G. Wier. 1994. Local stochastic release of Ca^{2+} in voltage-clamped rat heart cells: visualization with confocal microscopy. *J. Physiol. (Lond.).* 480:21–29.

Lopez-Lopez, J. R., P. S. Shacklock, C. W. Balke, and W. G. Wier. 1995. Local calcium transients triggered by single L-type calcium channel currents in cardiac cells. *Science.* 268:1042–1045.

Lukyanenko, V., I. Gyorke, and S. Gyorke. 1996. Regulation of calcium release by calcium inside the sarcoplasmic reticulum in ventricular myocytes. *Pflugers Arch.* 432:1047–1054.

Luo, C. H., and Y. Rudy. 1994. A dynamic model of the cardiac ventricular action potential. I. Simulations of ionic currents and concentration changes. *Circ. Res.* 74:1071–1096.

Marx, S. O., J. Gaburjakova, M. Gaburjakova, C. Henrikson, K. Ondrias, and A. R. Marks. 2001. Coupled gating between cardiac calcium release channels (ryanodine receptors). *Circ. Res.* 88:1151–1158.

Marx, S. O., S. Reiken, Y. Hisamatsu, T. Jayaraman, D. Burkhoff, N. Rosemblit, and A. R. Marks. 2000. PKA phosphorylation dissociates FKBP12.6 from the calcium release channel (ryanodine receptor): defective regulation in failing hearts. *Cell.* 101:365–376.

Mazhari, R., J. L. Greenstein, R. L. Winslow, E. Marban, and H. B. Nuss. 2001. Molecular interactions between two long-QT syndrome gene products, HERG and KCNE2, rationalized by in vitro and in silico analysis. *Circ. Res.* 89:33–38.

McDonald, T. F., A. Cavalie, W. Trautwein, and D. Pelzer. 1986. Voltage-dependent properties of macroscopic and elementary calcium channel currents in guniea pig ventricular myocytes. *Pflugers Arch.* 406: 437–448.

Michailova, A., and A. McCulloch. 2001. Model study of ATP and ADP buffering, transport of Ca^{2+} and Mg^{2+}, and regulation of ion pumps in ventricular myocyte. *Biophys. J.* 81:614–629.

Nabauer, M., G. Callewaert, L. Cleeman, and M. Morad. 1989. Regulation of calcium release is gated by calcium current, not gating charge, in cardiac myocytes. *Science.* 244:800–803.

Noble, D., A. Varghese, P. Kohl, and P. Noble. 1998. Improved guinea-pig ventricular cell model incorporating a diadic space, Ikr and Iks, and length- and tension-dependent processes. *Can. J. Cardiol.* 14:123–134.

O'Rourke, B., D. A. Kass, G. F. Tomaselli, S. Kaab, R. Tunin, and E. Marban. 1999. Mechanisms of altered excitation-contraction coupling in canine tachycardia-induced heart failure. I. Experimental studies. *Circ. Res.* 84:562–570.

Pandit, S. V., R. B. Clark, W. R. Giles, and S. S. Demir. 2001. A mathematical model of action potential heterogeneity in adult rat left ventricular myocytes. *Biophys J.* 81:3029–3051.

Parker, I., W. J. Zang, and W. G. Wier. 1996. Ca^{2+} sparks involving multiple Ca^{2+} release sites along Z-lines in rat heart cells. *J. Physiol. (Lond.).* 497:31–38.

Peterson, B., C. DeMaria, J. Adelman, and D. Yue. 1999. Calmodulin is the Ca^{2+} sensor for Ca^{2+}-dependent inactivation of L-type calcium channels. *Neuron.* 22:549–558.

Peterson, B. Z., J. S. Lee, J. G. Mulle, Y. Wang, M. de Leon, and D. T. Yue. 2000. Critical determinants of Ca^{2+}-dependent inactivation within an EF-hand motif of L-type Ca^{2+} channels. *Biophys. J.* 78:1906–1920.

Press, W. H., S. A. Teukolsky, W. T. Vetterling, and B. P. Flannery. 1992. Numerical Recipes. Cambridge University Press, Cambridge.

Priebe, L., and D. J. Beuckelmann. 1998. Simulation study of cellular electric properties in heart failure. *Circ. Res.* 82:1206–1223.

Rice, J. J., M. S. Jafri, and R. L. Winslow. 1999. Modeling gain and gradedness of Ca^{2+} release in the functional unit of the cardiac diadic space. *Biophys. J.* 77:1871–1884.

Rose, W. C., C. W. Balke, W. G. Wier, and E. Marban. 1992. Macroscopic and unitary properties of physiological ion flux through L-type Ca^{2+} channels in guinea-pig heart cells. *J. Physiol. (Lond.).* 456:267–284.

Sah, R., R. J. Ramirez, and P. H. Backx. 2002. Modulation of Ca^{2+} release in cardiac myocytes by changes in repolarization rate. Role of phase-1 action potential repolarization in excitation-contraction coupling. *Circ. Res.* 90:165–173.

Santana, L. F., H. Cheng, A. M. Gomez, M. B. Cannell, and W. J. Lederer. 1996. Relation between the sarcolemmal Ca^{2+} current and Ca^{2+} sparks and local control theories for cardiac excitation-contraction coupling. *Circ. Res.* 78:166–171.

Schiefer, A., G. Meissner, and G. Isenberg. 1995. Ca^{2+} activation and Ca^{2+} inactivation of canine reconstituted cardiac sarcoplasmic reticulum Ca^{2+}-release channels. *J. Physiol. (Lond.).* 489:337–348.

Schroder, F., R. Handrock, D. J. Beuckelmann, S. Hirt, R. Hullin, L. Priebe, R. H. Schwinger, J. Weil, and S. Herzig. 1998. Increased availability and open probability of single L-type calcium channels from failing compared with nonfailing human ventricle. *Circulation.* 98: 969–976.

Sham, J. S. K. 1997. Ca^{2+} release-induced inactivation of Ca^{2+} current in rat ventricular myocytes: evidence for local Ca^{2+} signaling. *J. Physiol.* 500:285–295.

Sham, J. S. K., L. Cleeman, and M. Morad. 1995. Functional coupling of Ca^{2+} channels and ryanodine receptors in cardiac myocytes. *Proc. Natl. Acad. Sci. USA.* 92:121–125.

Sham, J., L.-S. Song, Y. Chien, L.-H. Deng, M. D. Stern, E. G. Lakatta, and H. Cheng. 1998. Termination of Ca^{2+} release by a local inactivation of ryanodine receptors in cardiac myocytes. *Proc. Natl. Acad. Sci. USA.* 95:15096–15101.

Shannon, T. R., K. S. Ginsburg, and D. M. Bers. 2000. Reverse mode of the sarcoplasmic reticulum calcium pump and load-dependent cytosolic calcium decline in voltage-clamped cardiac ventricular myocytes. *Biophys. J.* 78:322–333.

Sipido, K., G. Callewaert, and E. Carmeliet. 1995. Inhibition and rapid recovery of Ca^{2+} during Ca^{2+} release from sarcoplasmic reticulum in guinea pig ventricular myocytes. *Circ. Res.* 76:102–109.

Smith, G. D., J. E. Keizer, M. D. Stern, W. J. Lederer, and H. Cheng. 1998. A simple numerical model of calcium spark formation and detection in cardiac myocytes. *Biophys. J.* 75:15–32.

Soeller, C., and M. B. Cannell. 1997. Numerical simulation of local calcium movements during L-type calcium channel gating in the cardiac diad. *Bipphys. J.* 73:97–111.

Song, L., J. Sham, M. Stern, E. Lakatta, and H. Cheng. 1998. Direct measurement of SR release flux by tracking "Ca^{2+} spikes" in rat cardiac myocytes. *J. Physiol.* 512:677–691.

Song, L.-S., S.-Q. Wang, R.-P. Xiao, H. Spurgeon, E. G. Lakatta, and H. Cheng. 2001. β-adrenergic stimulation synchronizes intracellular Ca^{2+} release during excitation-contraction coupling in cardiac myocytes. *Circ. Res.* 88:794–801.

Stern, M. D. 1992. Theory of excitation-contraction coupling in cardiac muscle. *Biophys. J.* 63:497–517.

Stern, M. D., L. S. Song, H. Cheng, J. S. Sham, H. T. Yang, K. R. Boheler, and E. Rios. 1999. Local control models of cardiac excitation-contraction coupling. A possible role for allosteric interactions between ryanodine receptors. *J. Gen. Physiol.* 113:469–489.

Sun, L., J.-S. Fan, J. W. Clark, and P. T. Palade. 2000. A model of the L-type Ca^{2+} channel in rat ventricular myocytes: ion selectivity and inactivation mechanisms. *J. Physiol. (Lond.).* 529:139–158.

Tseng, G.-N., R. B. Robinson, and B. F. Hoffman. 1987. Passive properties and membrane currents of canine ventricular myocytes. *J. Gen. Physiol.* 90:671–701.

Valdivia, H. H., J. H. Kaplan, G. C. Ellis-Davies, and W. J. Lederer. 1995. Rapid adaptation of cardiac ryanodine receptors: modulation by Mg^{2+} and phosphorylation. *Science.* 267:1997–2000.

Wagner, J., and J. Keizer. 1994. Effects of rapid buffers on Ca^{2+} diffusion and Ca^{2+} oscillations. *Biophys. J.* 67:447–456.

Wang, S. Q., L. S. Song, E. G. Lakatta, and H. Cheng. 2001. Ca^{2+} signaling between single L-type Ca^{2+} channels and ryanodine receptors in heart cells. *Nature.* 410:592–596.

Wier, W. G., and C. W. Balke. 1999. Ca^{2+} release mechanisms, Ca^{2+} sparks, and local control of excitation-contraction coupling in normal heart muscle. *Circ. Res.* 85:770–776.

Wier, W. G., T. M. Egan, J. R. Lopez-Lopez, and C. W. Balke. 1994. Local control of excitation-contraction coupling in rat heart cells. *J. Physiol.* 474:463–471.

Winslow, R. L., J. L. Greenstein, G. F. Tomaselli, and B. O'Rourke. 2001. Computational models of the failing myocyte: relating altered gene expression to cellular function. *Phil. Trans. R. Soc. Lond. A.* 359: 1187–1200.

Winslow, R. L., J. J. Rice, M. S. Jafri, E. Marban, and B. O'Rourke. 1999. Mechanisms of altered excitation-contraction coupling in canine tachycardia-induced heart failure. II. Model studies. *Circ. Res.* 84:571–586.

Yue, D. T., and E. Marban. 1990. Permeation in the dihydropyridine-sensitive calcium channel. Multi-ion occupancy but no anomalous mole-fraction effect between Ba^{2+} and Ca^{2+}. *J. Gen. Physiol.* 95:911–939.

Zahradnikova, A., and I. Zahradnik. 1996. A minimal gating model for the cardiac calcium release channel. *Biophys. J.* 71:2996–3012.

Zahradnikova, A., I. Zahradnik, I. Gyorke, and S. Gyorke, 1999. Rapid activation of the cardiac ryanodine receptor by submillisecond calcium stimuli. *J. Gen. Physiol.* 114:787–798.

Zuhlke, R., G. Pitt, K. Deisseroth, R. Tsien, and H. Reuter. 1999. Calmodulin supports both inactivation and facilitation of L-type calcium channels. *Nature.* 399:159–162.

Zygmunt, A. C. 1994. Intracellular calcium activates a chloride current in canine ventricular myocytes. *Am. J. Physiol. Heart Circ. Physiol.* 267: H1984–H1995.